Nucleic Acids Research, 2025, **53**, gkaf071
https://doi.org/10.1093/nar/gkaf071
Chemical Biology and Nucleic Acid Chemistry

Crosslinking pathways, dynamics, and kinetics between guanosine and lysine following one- versus two-electron oxidation of guanosine

May Myat Moe [1,2], Jonathan Benny [1,2], Varonica Lee [1], Midas Tsai [3], Jianbo Liu [1,2,*]

[1] Department of Chemistry and Biochemistry, Queens College of the City University of New York, 65-30 Kissena Blvd., Queens, NY 11367, United States
[2] Ph.D. Program in Chemistry, the Graduate Center of the City University of New York, 365 5th Ave., NY, NY 10016, United States
[3] Department of Natural Sciences, LaGuardia Community College, 31-10 Thomson Ave., Long Island City, NY 11101, United States

[*] To whom correspondence should be addressed. Email: jianbo.liu@qc.cuny.edu

Abstract

DNA–protein crosslinks (DPCs) remain as a poorly understood DNA lesion. Herein, crosslinking between guanosine and lysine was explored using a model system comprising 9-methylguanine (9MG) and CH_3NH_2. Crosslinking was induced by one-electron oxidized $9MG^{\bullet+}$ radical cations and doubly oxidized $[9MG - H_{N2}]^+$ cations, and analyzed as a function of reaction energy using an electrospray ionization tandem mass spectrometer. Experiment was augmented by dynamics simulations and kinetics modeling. Alongside the formation of $X\text{-}NH_2CH_3[9MG]^{\bullet+}$ (X = C2, C8) via direct addition, $8\text{-}CH_2NH_2[9MG + H_{N7}]^+$ was discovered as a new crosslink between $9MG^{\bullet+}$ and CH_3NH_2. This crosslink results from methyl–hydrogen abstraction of CH_3NH_2 by the N7 of $9MG^{\bullet+}$, followed by adding $^{\bullet}CH_2NH_2$ to $[9MG + H_{N7}]^+$. Notably, crosslinking is dramatically enhanced between $[9MG - H_{N2}]^+$ and CH_3NH_2, yielding major products $X\text{-}^+NH_2CH_3[9MG - H_{N2}]$ (X = N2, N3, C5, and C8, along with their proton tautomers), which form from the direct CH_3NH_2 addition to $[9MG - H_{N2}]^+$, and minor products $X\text{-}CH_2NH_2[9MG - H_{N2} + H_{O6}]^+$ (X = N2, N3, C5, N7, and C8), which arise from the combination of methyl–hydrogen abstraction products. This work dissected and distinguished the roles of one- versus two-electron oxidized guanosine in DPC formation, offering novel insights into oxidative DNA damage.

Graphical abstract

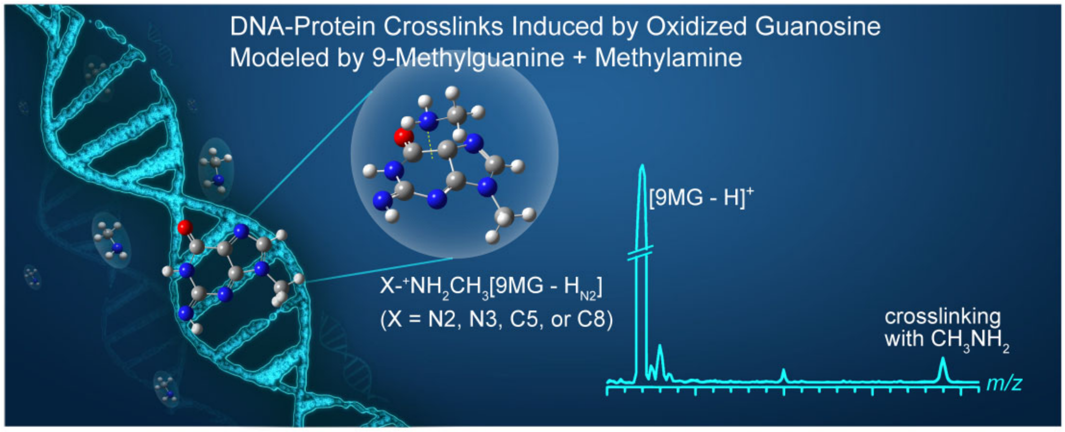

Introduction

Proteins bind to DNA during cellular activities such as replication, transcription, and repair [1, 2]. These interactions are precisely regulated and primarily non-covalent [3]. By contrast, DNA–protein crosslinks (DPCs) [4, 5] keep proteins covalently trapped. DPCs disrupt genomic integrity and contribute to mutagenesis and carcinogenesis by blocking replication and transcription [6], and they are difficult to repair due to bulky size [3]. DPCs can be induced by endogenous and exogenous sources [3]. Because of numerous intermediates and mechanisms that could be involved, DPCs remain one of the ubiquitous yet least understood forms of DNA damage [7, 8].

Guanosine (G) has the lowest oxidation potential (E°) among natural DNA nucleosides, with E° versus NHE (normal hydrogen electrode) increasing in the order of 1.29 V for guanosine <1.42 V for adenosine <1.6 V for cytidine <1.7 V for thymidine [9, 10]. Complementary pairing with cytidine in double-stranded DNA further lowers the E° of guanosine by 0.28–0.34 V

Received: December 9, 2024. **Revised:** January 21, 2025. **Editorial Decision:** January 23, 2025. **Accepted:** January 28, 2025

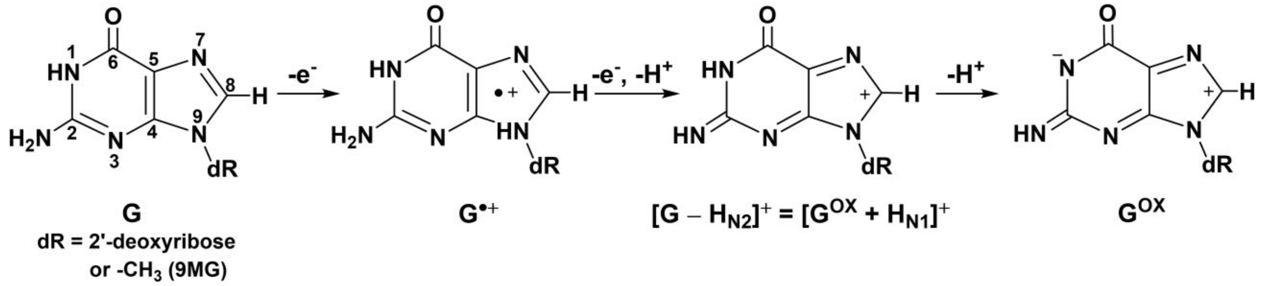

Scheme 1. One- and two-electron oxidation of guanosine.

[11, 12]. As a result, guanosine is a primary DNA target for one-electron oxidation upon photoionization [13], ionizing radiation [14], electron transfer with transition metals [15], electrocatalytic oxidation [16], photooxidation [17], etc. Holes generated at other nucleosides also migrate to guanosine sites [18]. Collectively, these factors render the formation of guanosine radical cations ($G^{\bullet+}$) the ultimate trap for oxidatively generated damage to DNA [19]. Formation of $G^{\bullet+}$ is the initial step in a cascade of biological sequelae [20–25]. For instance, $G^{\bullet+}$ serves as a precursor [26] to 8-oxoguanosine (OG)—the most commonly observed DNA lesion [27].

Following the formation of $G^{\bullet+}$ and OG, two mechanisms have been proposed for the formation of DPCs. The first mechanism involves the nucleophilic addition of an amino acid side chain, such as the ε-NH_2 of lysine (referred to as $LysNH_2$), to the C5 and C8 positions of $G^{\bullet+}$ or its deprotonated counterpart $[G - H]^{\bullet}$, as demonstrated by the groups of Cadet and Ravanat [28–31], Burrows [32, 33], and Stemp [34–36]. The second mechanism is driven by an oxidized OG intermediate, 2-amino-7,9-dihydro-purine-6,8-dione (OG^{OX}) [37, 38], which is highly susceptible to nucleophilic addition. Similar to the formation of guanidinohydantoin (Gh) and spiroiminodihydantoin (Sp) through the reaction of OG^{OX} with water [37, 38], OG^{OX}-mediated DPCs yield LysNH-Gh and LysNH-Sp, as reported by the groups of Burrows [32, 33, 39–42], Liu [43], and Merion [8].

DPCs were examined in various structural contexts, including nucleobases, oligonucleotides, and single- and double-stranded DNA. $LysNH_2$ was selected as the nucleophile due to its high abundance in DNA-coiling proteins (such as histones in eukaryotes [44]) and its proximity to guanosine residues [30, 40]. Depending on the specific DPC mechanisms under investigation, experiments incorporated type I [28–33] or II [8, 32, 33, 41] photooxidation, $Ir^{4+}/Fe^{3+}/Ru^{3+}$-induced oxidation [32–36, 40–42], the Fenton reaction [8], photoionization [45], or ionizing radiation [44]. These investigations were complemented by calculations of reaction potential energy surfaces conducted by the groups of Schlegel [46–48], Mishra [49], Barone [50], etc., and molecular dynamics simulations performed by the Dumont group [51, 52].

In the context of guanosine oxidation-induced DPCs, the potential for inducing DPCs via the doubly oxidized, non-radical cationic guanosine ($[G - H]^+$, Scheme 1) remains largely unexplored [48]. As a quinonoid species, $[G - H]^+$ (along with its neutral form G^{OX}) is predicted to react with amines and water at its C5 and C8 with minimal or no activation barriers [48, 53]. However, the contribution of $[G - H]^+$ to DPCs could not be directly assessed in aqueous experiments, as water effectively competes with $LysNH_2$ for addition to $[G - H]^+$ [48]. This limitation motivated us to investigate and compare DPCs induced by $G^{\bullet+}$ and $[G - H]^+$ in the gas phase. In a rarefied gaseous environment, the complexities and interferences present in solution are largely avoided, and $G^{\bullet+}$ and $[G - H]^+$ can persist for lifetimes several orders of magnitudes longer than in aqueous solution. This prolonged timeframe allows us to disentangle underlying processes and reveal intrinsic reactivities. In this sense, gas-phase experiments bridge gaps and resolve missing links in our understanding of DPC mechanisms.

In this work, 9-methylguanine (9MG) was used as a model compound for guanosine with the sugar moiety substituted by a methyl group, and methylamine, with E° similar to that of $LysNH_2$ [54], was employed as a nucleophile [46, 48]. By generating and isolating $9MG^{\bullet+}$ and $[9MG - H]^+$ in the gas phase, we were able to detect their distinct DPCs with methylamine through mass spectrometry measurements of individual product ions and cross sections. Reaction mechanisms and energetics were then analyzed on the basis of dynamics simulations, density functional theory (DFT) and coupled-cluster theory electronic structure calculations, and kinetics modeling.

Materials and Methods

Experimental details

Formation of $9MG^{\bullet+}$ and $[9MG - H]^+$ and their reactions with methylamine were conducted using a home-built tandem mass spectrometer coupled with electrospray ionization [55, 56]. A fresh solution of $[Cu^{II}(9MG)_{1-3}]^{\bullet 2+}$ was prepared by mixing 0.25 mM 9MG (Chemodex, >98%) and 0.25 mM $Cu(NO_3)_2$ (Alfa Aesar, 99.999%) in methanol/water (3:1 v/v). The solution was electrosprayed into the source chamber of the mass spectrometer via a desolvation capillary heated to 190°C and biased at 130 V relative to ground. A skimmer was positioned 3 mm away from the capillary exit and biased at 85 V. The electric field between the capillary exit and the skimmer facilitated the generation of $9MG^{\bullet+}$ radical cations via a collision-induced electron-transfer reaction $[Cu^{II}(9MG)_3]^{\bullet 2+} \rightarrow [Cu^{I}(9MG)_2]^+ + 9MG^{\bullet+}$ [56–60]. $[9MG - H]^+$ was produced for the first time via $9MG^{\bullet+} \rightarrow [9MG - H]^{\bullet} + H^+$ followed by $[9MG - H]^{\bullet} + 9MG^{\bullet+} \rightarrow [9MG - H]^+ + 9MG$ (see details in Supplementary Figure S1 and Supplementary Information).

Ions were thermalized to 310 K through collisional cooling and kinetic energy dumping within a radiofrequency hexapole ion guide. Ions of interest were mass selected using a quadrupole mass filter, followed by collimation into an octopole ion guide. The octopole ion guide trapped ions radially and guided them through a scattering cell that encircles the central 11 cm of the octopole, which contained deuterated CD_3NH_2 gas (Cambridge Isotope Laboratories, D_3 98%). A DC (direct current) bias on the octopole set kinetic energies for reactant ions in the laboratory frame (E_{lab}), which determined ion-molecule collision energy (E_{CM}) in the center-of-mass frame using $E_{\mathrm{CM}} = E_{\mathrm{lab}} \times m_{\mathrm{neutral}} / (m_{\mathrm{ion}} + m_{\mathrm{neutral}})$, where m_{ion} and m_{neutral} represent the masses of ionic and neutral reactants, respectively. Product ions and unreacted reactant ions were collected by the octopole, passed into a second quadruple mass filter for analysis, and counted by a pulse-counting electron multiplier. The CD_3NH_2 gas pressure within the scattering cell was maintained at 0.01–0.015 mTorr to ensure that each reactant ion experienced, at most, a single collision with CD_3NH_2. Under these conditions, absolute product cross sections could be calculated using the Beer–Lambert law [55, 56, 61].

Primary ions were generated at intensities of 5×10^5 counts/s for $9MG^{\bullet+}$ and 2×10^3 counts/s for $[9MG - H]^+$. Both first and second quadrupole mass filters used ΔM as a control for mass resolution. The purity of mass-selected reactant ion beam was verified, with no leakage or background ions detected at the M ± 1 positions of the reactant ion. Random background ion was <1 count every 20 s. The full width at half maximum of E_{lab} was measured to be ≤0.65 eV using retarding potential analysis [55, 62], corresponding to a spread of ∼ 0.1 eV in nominal E_{CM}. E_{CM} was scanned from 0.05 to 2.0 eV for each reaction to capture complex-mediated mechanism at low energies and direct mechanism at high energies. All measurements were repeated at least three times. The relative uncertainty in cross section measurements was estimated to be below 5%.

For endothermic reactions, threshold energy (E_0) at 0 K was determined by fitting kinetic energy-dependent product ion cross section to a modified line-of-centers (LOC) model [63, 64]: $\sigma(E_{\mathrm{CM}}) = \sigma_0(E_{\mathrm{CM}} + E_{\mathrm{vib}} + E_{\mathrm{rot}} - E_0)^n / E_{\mathrm{CM}}$, where σ_0 is a normalization factor, E_{vib} and E_{rot} are reactants vibrational and rotational energies, and n is a fitting parameter determining the efficiency of kinetic energy in driving the reaction. To account for the spread of nominal E_{CM} and Boltzmann distributions of E_{vib} and E_{rot}, as well as Doppler broadening [65] and reaction kinetic shift [66] in the beam experiment, the LOC model was integrated into an in-house Monte Carlo ion-molecule collision simulation program [67, 68]. E_0 was derived from a simulation that best matched experimental cross section.

Computations

(1) Molecular dynamics: Quasi-classical direct dynamics trajectory (QCT) simulations were performed using VENUS [69, 70] to set up initial conditions mimicking experiment and using Gaussian 16 [71] to propagate trajectory. Classical equations of motion were solved using a Hessian-based predictor-corrector algorithm [72] with a step size of 0.25 $(\mathrm{amu})^{1/2}$·Bohr (equivalent to 0.4 fsec trajectory time). Hessian was updated every five steps. To balance computational accuracy and efficiency, the ωB97XD [73] functional paired with the 6-31G(d) basis set was chosen for calculations. This functional minimizes self-interaction errors and provides an accurate description of radicals [74, 75], as demonstrated in similar reactions [76, 77]; and the energy accuracy of ωB97XD/6-31G(d) is within 0.1 eV compared to that of ωB97XD/6-31+G(d,p).

Each trajectory began at an ion-neutral distance of 10 Å to ensure no initial interaction between the randomly oriented partners. Reactants were initiated at 300 K by sampling quasi-classical Boltzmann distributions of E_{vib} and E_{rot} [78]. Relative velocities, aligned with E_{CM} and impact parameter b, were added to the reactants. The purpose of the simulations was to identify important products, short-lived intermediates, and transition states (TSs). Therefore, trajectories were calculated at $b = 0.1$ Å (rather than randomly sampling b within the maximum collision radius) and $E_{\mathrm{CM}} = 0.05$ or 0.1 eV to enhance the likelihood of capturing reactive trajectories. The trajectory terminated at 2500 (or 4000) fsec or when products had separated by 10 Å.

(2) Reaction energetics: Structures of reactants, intermediates, TSs, and products were re-optimized at the ωB97XD/6-31+G(d,p) level of theory. Their Cartesian coordinates are provided in Supplementary Information. Vibrational frequencies were computed to confirm stationary structures (no imaginary frequency) and TSs (with only a single imaginary frequency). Intrinsic reaction coordinate was calculated to validate TSs connecting to correct products. For singlet diradicals, broken symmetry unrestricted SCF with "guess = mix" was used to mix HOMO and LUMO and break α–β and spatial symmetries in initial guesses [79]. Energies of diradicals were spin-purified using Yamaguchi's approximate spin projection [80–83]: $E = \frac{\langle \hat{S}^2 \rangle^{\mathrm{HS}}}{\langle \hat{S}^2 \rangle^{\mathrm{HS}} - \langle \hat{S}^2 \rangle^{\mathrm{BS}}} E^{\mathrm{BS}} - \frac{\langle \hat{S}^2 \rangle^{\mathrm{BS}}}{\langle \hat{S}^2 \rangle^{\mathrm{HS}} - \langle \hat{S}^2 \rangle^{\mathrm{BS}}} E^{\mathrm{HS}}$, where E^{BS} and $\langle \hat{S}^2 \rangle^{\mathrm{BS}}$ denote the energy and the expectation value of total spin angular momentum operator for the broken-symmetry singlet, and E^{HS} and $\langle \hat{S}^2 \rangle^{\mathrm{HS}}$ denote corresponding values for the triplet. As shown in Supplementary Table S6, the degree of spin contamination before projection is minor. All calculated reaction enthalpies (ΔH, 298 K) include zero-point energy (ZPE, scaled by 0.975 [84]) and thermal correction.

Energies of the DFT-optimized structures were cross-checked using the domain-based local pair-natural orbital coupled cluster single-, double-, and perturbative triple excitation method DLPNO-CCSD(T) [85, 86] paired with the aug-cc-pVQZ basis set. The calculations were carried out using ORCA 4.2.1 [87, 88] and results are reported in Supplementary Tables S1–S6. In general, DLPNO-CCSD(T) predicted reaction energetics 0.2–0.3 eV higher than ωB97XD.

(3) Unimolecular kinetics: Rice–Ramsperger–Kessel–Marcus (RRKM) [89] rate constants (k) were calculated using the code by Zhu and Hase [90], with the density of states evaluated using a direct count algorithm [91]. Since no reverse barriers exist for crosslinking, orbit TSs [92] were assumed with the reaction orbital angular momentum (L) estimated from the collision cross section ($\sigma_{\mathrm{collision}}$), i.e. $L = \mu \cdot \nu \cdot \sqrt{\sigma_{\mathrm{collision}}/\pi}$, where μ is the reduced mass and ν is the relative velocity of collision partners.

Experimental Results

Products of $9MG^{\bullet +}$ with CD_3NH_2

The CD_3NH_2 isotope combination was used to identify the sources of H abstraction in the products. Hydrogen atom scrambling (i.e. H/D exchange) between reactant ions and -CD_3 can also provide supplementary evidence for complex mediation in the reaction, in addition to the observation of crosslinking products. The following product channels were detected for $9MG^{\bullet +}$ (m/z 165) + CD_3NH_2:

$m/z\,34$:	$CD_3NH_2^{\bullet +} + 9MG$	charge transfer = CT
$m/z\,35$:	$CD_3NH_3^{+} + [9MG - H]^{\bullet}$	proton transfer = PT
$m/z\,166$:	d_1-$9MG^{\bullet +} + CHD_2NH_2$	H/D exchange = H_Ex
	$[9MG + H]^{+} + CD_3NH^{\bullet}$	amine-H abstraction = HA_NH$_2$
$m/z\,167$:	$[9MG + D]^{+} + {}^{\bullet}CD_2NH_2$	methyl-H abstraction = HA_CD$_3$
$m/z\,199$:	crosslinking adduct	DPC

A representative product ion mass spectrum, recorded at $E_{CM} = 0.05$ eV, is shown in Fig. 1A. Individual product ion cross sections were measured across an E_{CM} range from 0.05 to 2.0 eV and are represented by red traces in Fig. 1B–F. Error bars represent standard deviations. The sum of all product ion cross sections (σ_{total}) and reaction efficiency are presented in Fig. 1G. The σ_{total} reaches a maximum of 17 Å at $E_{CM} = 0.05$ eV, gradually decreases to 6 Å at 0.3 eV, and then nearly levels off at higher energies. Reaction efficiency was calculated as $\sigma_{total}/\sigma_{collision}$, where $\sigma_{collision}$ was determined from either the ion-neutral capture cross section using a statistical adiabatic channel model [93] or the hard-sphere collision cross section based on orientation-averaged projected area [94, 95], whichever is greater. Reaction efficiency is maximized (7%) at $E_{CM} = 0.1$ eV, decreases to 5% at 0.3 eV, and remains nearly constant at higher energies. The dip in reaction efficiency at 0.05 eV is an artifact caused by back-scattering of some product ions at the lowest E_{CM}, leading to their absence from product ion detection.

(1) ***CT and PT***: The cross sections for CT and PT present a threshold at low energies and increase monotonically with rising E_{CM} (Fig. 1B and C). By accounting for reaction energy broadening and kinetic shift, the blue-line LOC fits successfully reproduced experimental cross sections. From the LOC fits, the 0 K reaction threshold was determined to be 1.5 ± 0.2 eV for CT and 0.6 ± 0.1 eV for PT. The uncertainties in E_0 were estimated from multiple LOC fits over an acceptable range of n and included uncertainty in E_{CM}, with the best fits achieved at $n = 2.4$–2.5.

Using literature-reported adiabatic ionization potentials (AIPs), i.e. AIP(CH_3NH_2) = 9.04 eV [96] and AIP(9MG) = 7.63 eV [83], we calculated ΔH (0 K) of 1.41 eV for CT. This value agrees well with the experimental E_0. The G4(MP2)-6X-calculated gas-phase acidity for $9MG^{\bullet +}$ is 10.0 eV for N1H, 9.9 eV for N2H$_a$, and 10.1 eV for N2H$_b$ [97]. The NIST-listed basicity for CH_3NH_2 is 9.32 eV [98]. Combining these data leads to a PT threshold in the range of 0.58–0.78 eV, with the PT from N2H$_a$ (with $\Delta H = 0.58$ eV) best matching the experiment.

(2) ***H_Ex and HA_NH$_2$***: The two reactions yielded the same product ion m/z 166; however, they could be distinguished through kinetic-energy dependence. The cross section in Fig. 1D consists of two components: the first component reaches a maximum at the lowest E_{CM} and decreases gradually with increasing E_{CM}, which well matches the thermal-neutral H_Ex; while the second component grows at high energies and becomes energy independent at $E_{CM} = 1.0$–2.0 eV, which matches the endothermic HA_NH$_2$. To distinguish individual contributions, we modeled the H_Ex cross section using the ion-dipole capture cross section [93] and the HA_NH$_2$ cross section using the modified LOC model, matching their sum to the experimental data. The LOC-fitted E_{CM}-dependence for H_Ex of $9MG^{\bullet +}$ + CD_3NH_2 resembles that for $9MG^{\bullet +}$ + D_2O [76]. The LOC fitting for HA_NH$_2$ yields a threshold <0.4 eV.

(3) ***HA_CD$_3$*** : Opposite to amine-H abstraction, the cross section for hydrogen abstraction from CD_3 increases with decreasing E_{CM} (Fig. 1E), indicating an exothermic pathway with no activation barrier above the reactants. The cross section reaches a maximum of 4 Å^2 at $E_{CM} = 0.05$ eV, then declines to 2 Å^2 at 1.2 eV before becoming energy independent at higher E_{CM}. While the contribution of double H/D exchange to the product ions m/z 167 is possible, it is unlikely to be significant. This is supported by the fact that double H/D exchange was not observed in the reaction of $9MG^{\bullet +}$ + D_2O, which was measured over a similar E_{CM} range using the same mass spectrometer [76].

(4) ***Crosslinking***: DPCs represent the most important product channel. It shows sharp E_{CM} suppression with a maximum cross section of 6 Å^2 at 0.05 eV, declining to 1 Å^2 at 0.15 eV and becoming negligible starting at 0.3 eV (Fig. 1F). This pattern agrees with a reaction governed by a complex. The inset in Fig. 1F illustrates the product branching ratio for crosslinking. It decreases from 0.4 at $E_{CM} = 0.05$ eV to 0.1 at 0.2 eV, eventually approaching near zero at 0.4 eV and beyond. For comparison, the branching ratio for HA_NH$_2$ + H_Ex is 0.44 at $E_{CM} = 0.05$–0.1 eV and increases to 0.60 at 0.4 eV. The branching ratio for HA_CD$_3$ is 0.24 at $E_{CM} = 0.05$ eV and increases to 0.32–0.35 at 0.1–0.4 eV.

Products of $[9MG - H]^{+}$ with CD_3NH_2

This work generated, separated, and measured $[9MG - H]^{+}$ for the first time. The reaction of $[9MG - H]^{+}$ with CD_3NH_2 was assessed using a procedure similar to that for $9MG^{\bullet +}$ + CD_3NH_2. The mass spectrum shown in Fig. 2A displays product ions

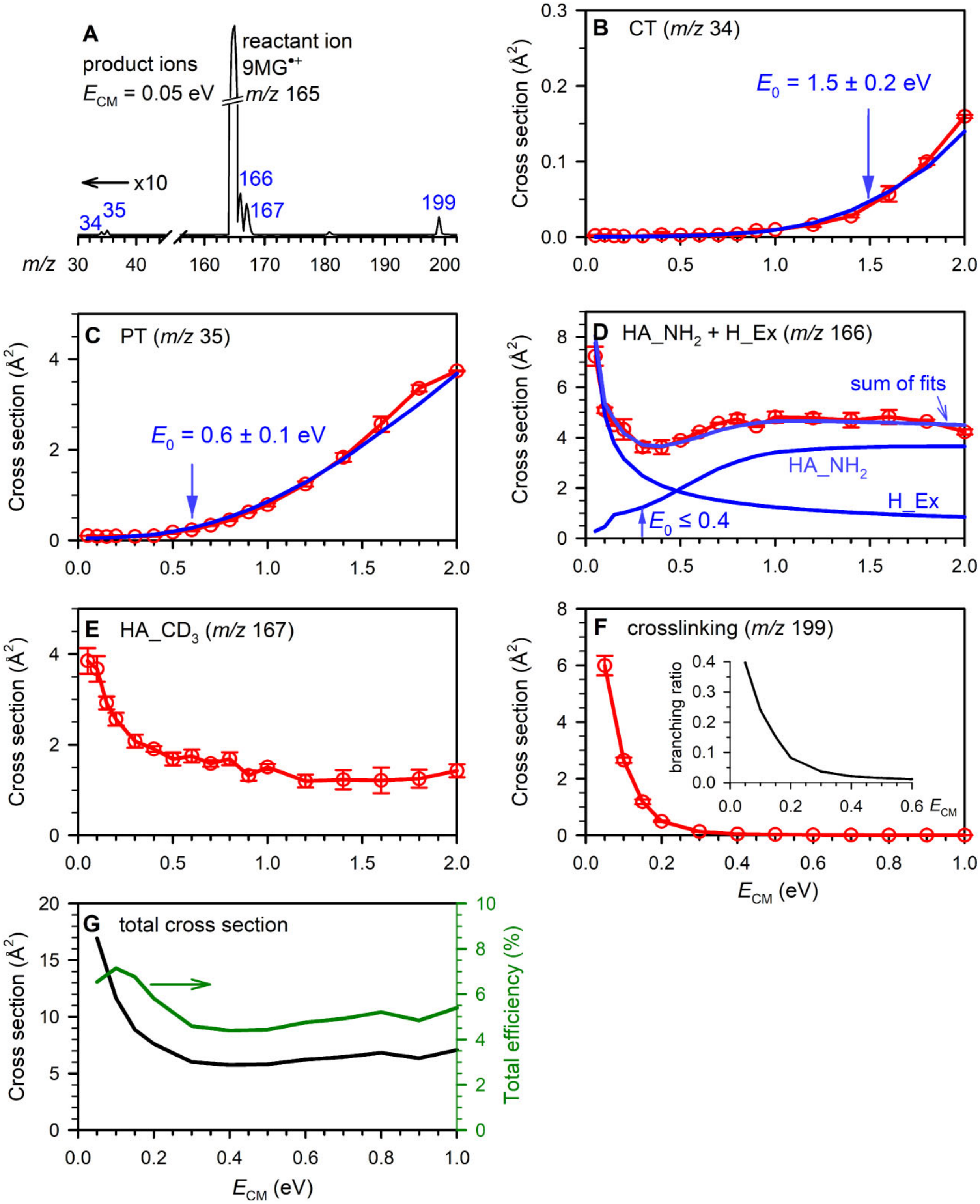

Figure 1. (**A**) Product ion mass spectrum for the reaction of $9MG^{\bullet+}$ + CD_3NH_2, with the intensities of CT and PT product ions scaled by a factor of 10; (**B–F**) cross sections for individual product ions as a function of E_{CM}, where red plots represent experimental data and blue lines represent LOC fits. The inset in panel (**F**) shows the branching ratio for crosslinking; (**G**) total product cross section (left axis) and reaction efficiency (right axis) as a function of E_{CM}.

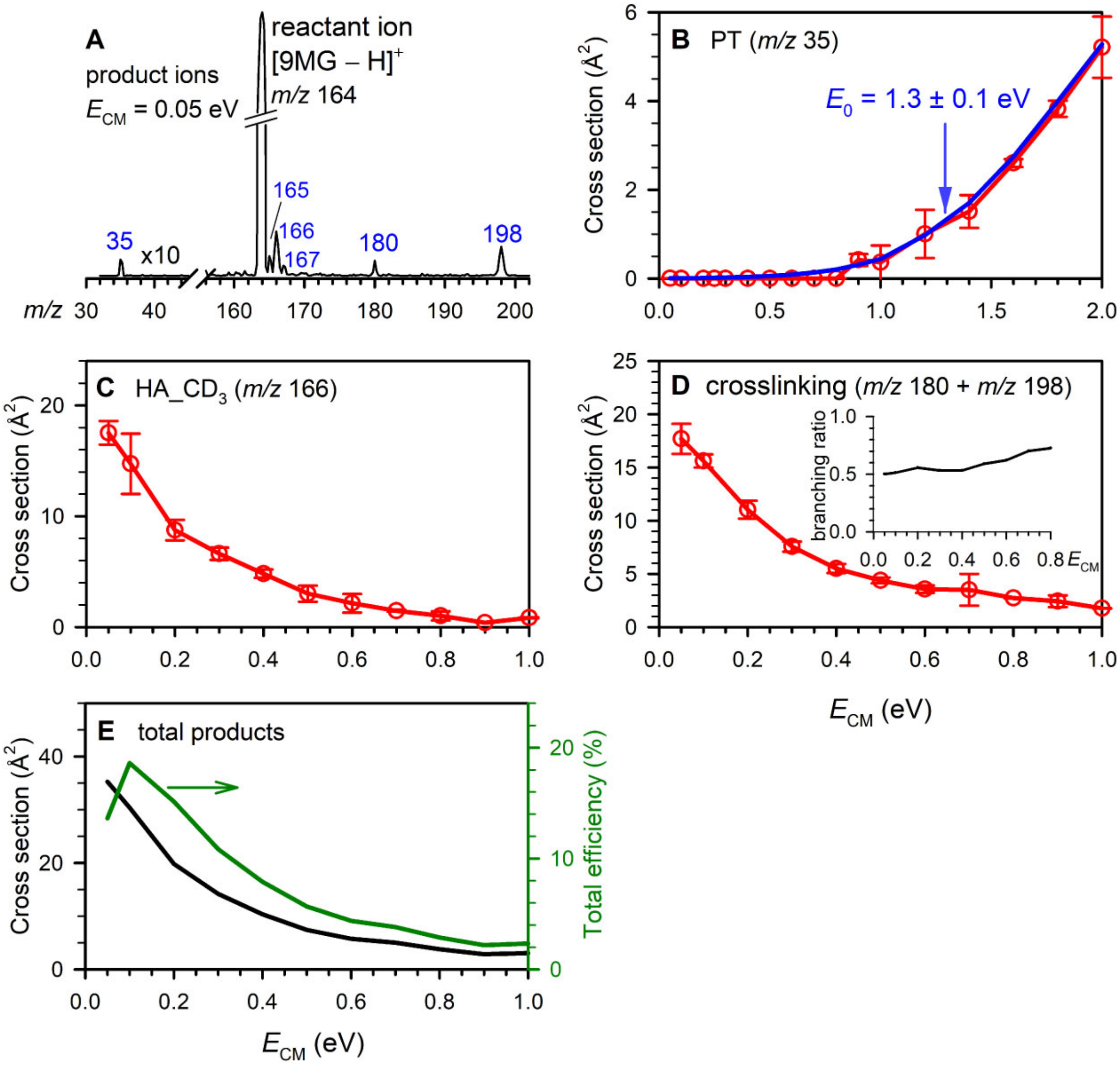

Figure 2. (**A**) A product ion mass spectrum for the reaction of [9MG – H]$^+$ + CD_3NH_2, with the PT product ion intensities scaled by a factor of 10; (**B**–**D**) cross sections for individual product ions as a function of E_{CM}, where red plots represent experimental data, and blue line represents a LOC fit. The insert in panel (D) shows the branching ratio for crosslinking; (**E**) total product cross section (left axis) and reaction efficiency (right axis) as a function of E_{CM}.

measured at $E_{CM} = 0.05$ eV:

$m/z\,35$:	$CD_3NH_3{}^+ + 9MG^{OX}$	PT
$m/z\,165$:	d_1-$[9MG - H]^+ + CHD_2NH_2$	H_Ex
	$9MG^{\bullet+}$tautomers $+ CD_3NH^{\bullet}$	HA_NH_2
$m/z\,166$:	d_1-$9MG^{\bullet+}$tautomers $+ {}^{\bullet}CD_2NH_2$	HA_CD_3
$m/z\,167$:	d_1-$[9MG + H]^+$tautomers $+ CD_2NH$	$H^{\ominus}A$ + PT
$m/z\,198$:	crosslinking adduct	DPC

Many product channels are similar to those observed in the reaction of $9MG^{\bullet+}$+ CD_3NH_2, such as PT, H_Ex, HA_NH_2, HA_CD_3, and DPC. Products that are specific to [9MG – H]$^+$ include m/z 167 that corresponds to d_1-[9MG + H]$^+$ tautomers formed via sequential hydride abstraction ($H^{\ominus}A$) and proton transfer, and m/z 180 that corresponds to CD_3 elimination from an adduct (indicating that certain crosslinking pathways release enough energy to eliminate the methyl group). The intensities of m/z 180 are thus lumped into the crosslinking cross sections. Figure 2B–D presents individual product channels across the E_{CM} range of 0.05–2.0 eV, except for m/z 165 and 167 as their cross sections were too low to make meaningful measurements.

The two major product channels, HA_CD_3 and crosslinking, are both exothermic, reaching a maximum at the lowest E_{CM} and gradually decreasing to a minimum at 1.0 eV. The LOC-fitted E_0 for the PT reaction is 1.3 ± 0.1 eV with $n = 2.4$ (Figure 2B). At first glance, it may seem surprising that CT was absent for [9MG – H]$^+$ + CD_3NH_2, despite it being only endothermic by 0.6 eV. However, the CT product pair, ^{2}[9MG – H]$^{\bullet}$ + $^2CD_3NH_2^{\bullet+}$, once formed, would readily undergo proton transfer barrierlessly to yield d_1-9MG$^{\bullet+}$ + $^{\bullet}CD_2NH_2$.

Notably, the reaction efficiency for [9MG – H]$^+$ with CD_3NH_2 reaches 19% at low energy (Fig. 2E), which is more than twice that for 9MG$^{\bullet+}$. Furthermore, the cross section for methyl-H abstraction by [9MG – H]$^+$ is five times higher than that by 9MG$^{\bullet+}$. The crosslinking for [9MG – H]$^+$ is three times greater than that for 9MG$^{\bullet+}$. The product branching ratio for crosslinking in the [9MG – H]$^+$ reaction reaches 0.5 at $E_{CM} = 0.05$ eV and increases to 0.75 at 0.8 eV (while that for HA_CD_3 decreases from 0.5 at 0.05 eV to 0.25 at 0.8 eV). In contrast, the crosslinking branching ratio in the 9MG$^{\bullet+}$ reaction is only 0.4 at 0.05 eV and rapidly decreases to near zero at 0.6 eV. It suggests that [9MG – H]$^+$ is more susceptible to DPCs. It also suggests that the crosslinking of [9MG – H]$^+$ involves complex-mediated pathways at low energies and direct addition at high energies.

Molecular Dynamics Trajectory Results

To probe the origin of the DPC enhancement by [9MG – H]$^+$, dynamics simulations were utilized to mimic the crosslinking of CH_3NH_2 with 9MG$^{\bullet+}$ versus [9MG – H]$^+$. Direct dynamics simulations [99] do not require a predefined potential surface. Instead, trajectories calculate energies, force constants, and Hessians “on the fly.” This approach allows for the inclusion of all energetically accessible reacting structures, so that trajectories can reveal preferred pathways. A total of 800 trajectories were calculated for 9MG$^{\bullet+}$ + CH_3NH_2 and 400 trajectories for [9MG – H]$^+$ + CH_3NH_2. All trajectories were simulated at 0.05 or 0.1 eV to exclude endothermic CT and PT, as they are not directly relevant to DPCs.

9MG$^{\bullet+}$ + CH_3NH_2

Four reactive trajectory pathways were identified for 9MG$^{\bullet+}$ + CH_3NH_2. These include HA_CH_3, HA_NH_2, N-terminal addition of CH_3NH_2 to the C2 of 9MG$^{\bullet+}$, and N-terminal addition of CH_3NH_2 to the C8 of 9MG$^{\bullet+}$. Fig. 3 illustrates individual pathways. For each trajectory, the top frame presents changes in reaction potential energy (PE, left axis) and center-of-mass reactant/product distance (CM separation, right axis) throughout the trajectory, and the bottom frame presents variations of reactive bond lengths. The high-frequency oscillations in PEs and bond lengths reflect vibrations and rotations of reactants and products. The first turning point in the CM separation marks the time at which the ion and molecule start to collide, which often introduces a change in PE.

(1) ***Hydrogen abstraction pathways***: HA_CH_3 represents the most common trajectory outcome with a probability of 10 ± 1%. As shown in Fig. 3A, methyl-H abstraction [defined as point when the new r(9MG)N7-H bond forms] occurs immediately upon collision. Subsequently, a product-like complex forms, as indicated by the oscillation of the product CM distance around 5 Å. This complex does not maintain a well-defined geometry but undergoes significant intermolecular motion, as evidenced by multiple turning points in the relative motion of the product CM. Although the simulation lasted only 2500 fsec, the actual ion time-of-flight within the mass spectrometer was around 10^2 µs. This extended time allowed the H-abstraction product to repeatedly encounter and find an optimal orientation for a subsequent addition reaction. A similar phenomenon occurred in the HA_NH_2 trajectory (Fig. 3B), despite this being a minor channel with a trajectory probability of 1 ± 0.4%.

(2) ***Direct addition pathways***: The C2- and C8-addition of CH_3NH_2 account for 1 ± 0.4% and 2 ± 0.5% of all trajectories, respectively. The time required for addition varies depending on the initial collision orientation, e.g. the formation of the 2-NH_2CH_3[9MG]$^{\bullet+}$ adduct (Fig. 3C) occurs 1700 fsec after the collision, while the formation of 8-NH_2CH_3[9MG]$^{\bullet+}$ (Fig. 3D) occurs 600 fsec after the collision.

[9MG – H]$^+$ + CH_3NH_2

(1) ***Direct addition pathways***: Trajectories for [9MG – H]$^+$ + CH_3NH_2 are dominated by the formation of 2-$^+NH_2CH_3$[9MG – H_{N2}] (followed by proton tautomerization to 2-$NHCH_3$[9MG – H_{N2} + H_{N3}]$^+$, Fig. 4A, yield = 3 ± 0.9%), 5-$^+NH_2CH_3$[9MG – H_{N2}] (Fig. 4B, 24 ± 2%), and 8-$^+NH_2CH_3$[9MG – H_{N2}] (Fig. 4C, 37 ± 2%). Unlike the addition of 9MG$^{\bullet+}$ + CH_3NH_2 which occurs significantly later after the collision, the addition of CH_3NH_2 to [9MG – H]$^+$ takes place immediately upon collision, as seen from the CM separation and the rapid formation of new bonds. A significant decrease in PE upon addition indicates that the process is highly exothermic.

(2)***Sequential methyl hydride abstraction (H$^{\ominus}$A_CH_3) and PT***: This pathway accounts for a small fraction (2 ± 0.7%) of the trajectories. As exemplified in Fig. 5A–B, the C5 of [9MG – H]$^+$ abstracts a hydride anion from the methyl group of CH_3NH_2, followed by PT from $CH_2{}^+NH_2$ to the N2 or N7. Hydride abstraction and PT are separated by 650–850 fsec in the trajectory and are distinguished by accompanying charge transfer. The final products contribute to the m/z 167 peak in Fig. 2A.

In summary, the trajectories successfully reproduced all experimental products and their relative importance, except for the open-shell H abstraction for [9MG – H]$^+$ + CH_3NH_2, as the QCT trajectories remained in the initial closed-shell singlet state. Moreover, the trajectories correctly predicted a significantly higher overall reactivity and crosslinking yield of [9MG – H]$^+$ compared to 9MG$^{\bullet+}$. This indicates that direct dynamics simulations effectively captured key reaction dynamics and outcomes and can therefore be used to extract mechanistic insights.

Analysis of Crosslinking Pathways and Kinetics

Guided by trajectory results, reaction coordinates were constructed for all probable pathways at the ωB97XD/6-31+G(d,p) level of theory. To complete a comprehensive and reliable kinetics analysis, we included not only primary intermediates and products in the calculations but also downstream conversions.

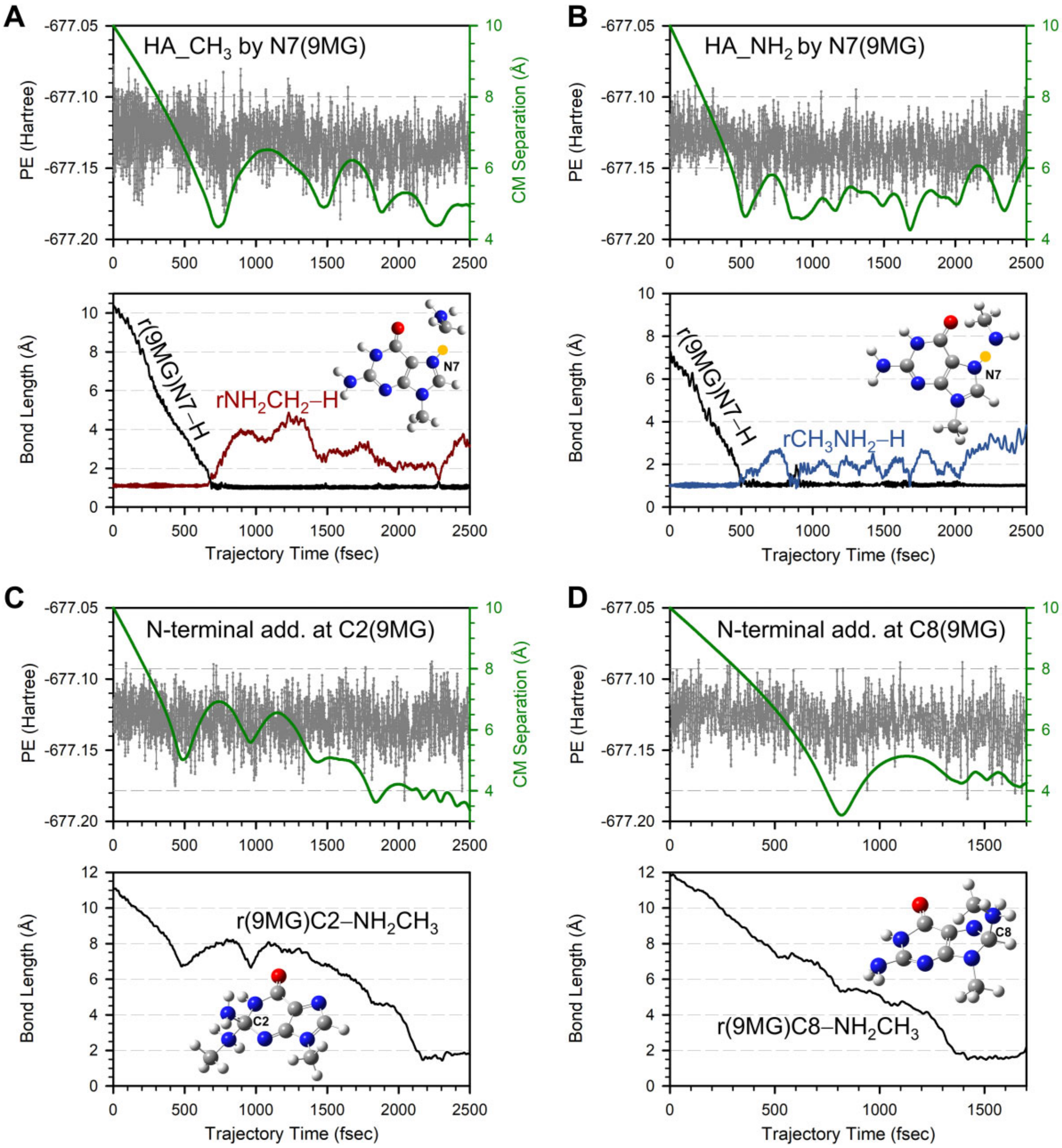

Figure 3. Trajectories for the reaction of $9MG^{\bullet+}$ + CH_3NH_2 simulated at $E_{CM} = 0.05$ eV, showing (**A**) methyl-H abstraction, (**B**) amine-H abstraction, (**C**) N-terminal addition of CH_3NH_2 to C2 in $9MG^{\bullet+}$, and (**D**) N-terminal addition of CH_3NH_2 to C8 in $9MG^{\bullet+}$. Each top frame depicts changes of potential energy (left axis) and center-of-mass reactant/product separation (right axis), while the bottom frame shows reactive bond lengths throughout the trajectory. Inset snapshots illustrate product structures, with the abstracting H highlighted in yellow.

$9MG^{\bullet+}$ mediates DPCs with CH_3NH_2 primarily by methyl-H abstraction and direct addition

(**1**) ***Intermediacy of HA_CH₃***: The dominance of HA_CH₃ in both experiment and trajectories motivated us to investigate all possible methyl-H abstraction pathways. The results are summarized in Scheme 2A and Supplementary Scheme S1, and reactions (1.1–1.3). Given that methyl-H abstraction was measured to be exothermic, only reaction (1.1) is important.

$$9MG^{\bullet+} + CH_3NH_2 \rightarrow$$

$$[9MG + H_{N7}]^{+}\cdots{}^{\bullet}CH_2NH_2 \quad \Delta H = -0.88\,\text{eV},\ \text{TS} = -0.74\,\text{eV} \rightarrow [9MG + H_{N7}]^{+} + {}^{\bullet}CH_2NH_2 \quad \Delta H = -0.14\,\text{eV} \quad (1.1)$$

$$[9MG + H_{O6}]^{+}\cdots{}^{\bullet}CH_2NH_2 \quad \Delta H = -0.69\,\text{eV},\ \text{TS} = -0.71\,\text{eV} \rightarrow [9MG + H_{O6}]^{+} + {}^{\bullet}CH_2NH_2 \quad \Delta H = 0.18\,\text{eV} \quad (1.2)$$

$$[9MG + H_{N3}]^{+}\cdots{}^{\bullet}CH_2NH_2 \quad \Delta H = 0.02\,\text{eV},\ \text{TS} = 0.22\,\text{eV} \rightarrow [9MG + H_{N3}]^{+} + {}^{\bullet}CH_2NH_2 \quad \Delta H = 0.66\,\text{eV} \quad (1.3)$$

Since d_3-methylamine was used in the experiment, the kinetic isotope effect (KIE) was evaluated. Using RRKM theory, the k_H and k_D for reaction (1.1) were calculated, yielding a k_H/k_D ratio of 4 and 5 in the E_{CM} range of 0.05–0.3 eV. This indicates that methyl-H abstraction is significantly suppressed by deuteration. We also calculated tunneling effect for methyl-H abstraction

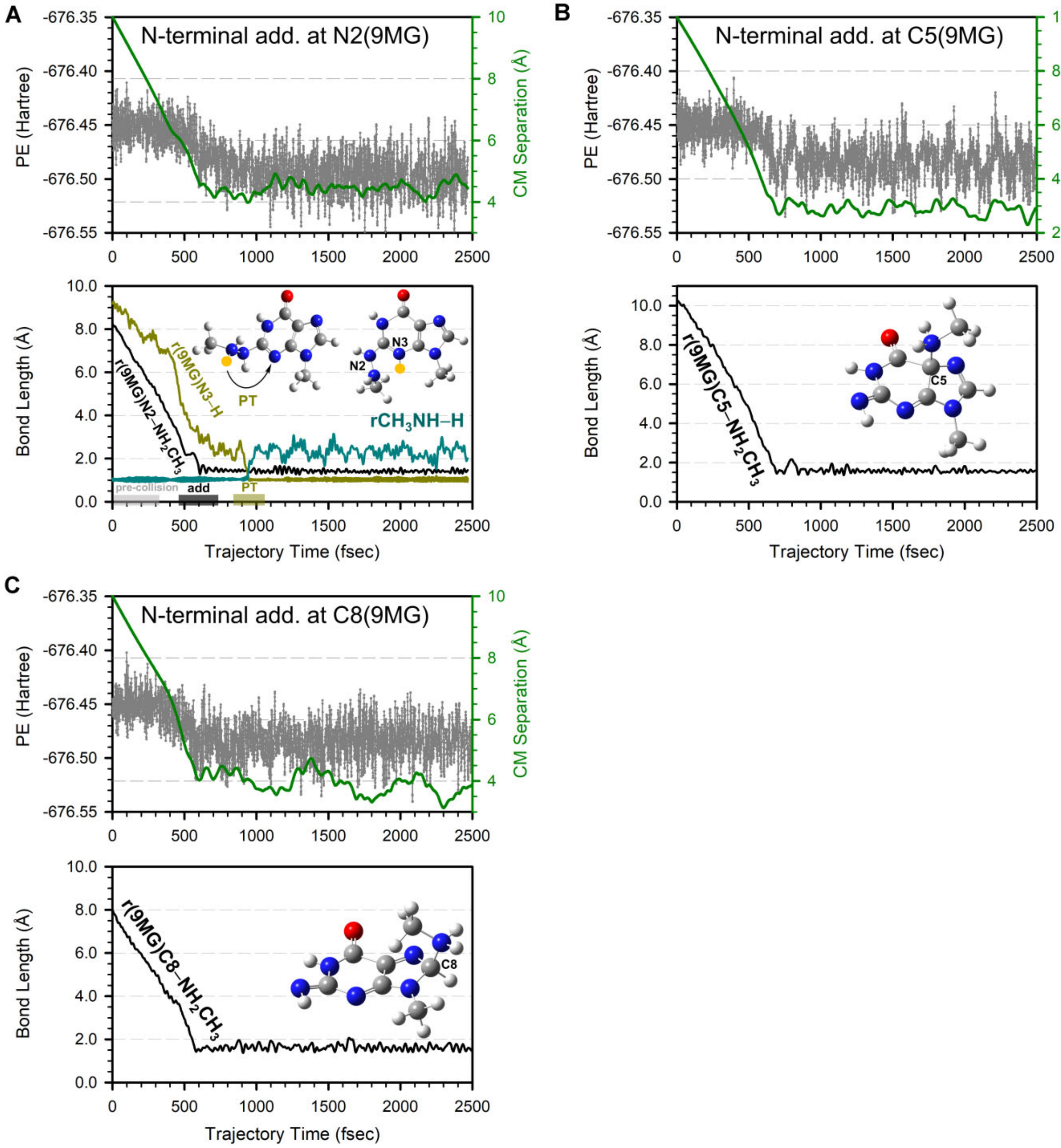

Figure 4. Trajectories for direct addition of $[9MG - H]^+ + CH_3NH_2$ simulated at $E_{CM} = 0.1$ eV, leading to the formation of (**A**) $2\text{-}NHCH_3[9MG - H_{N2} + H_{N3}]^+$, (**B**) $5\text{-}^+NH_2CH_3[9MG - H_{N2}]$, and (**C**) $8\text{-}^+NH_2CH_3[9MG - H_{N2}]$. Each top frame depicts the changes of potential energy (left axis) and center-of-mass reactant/product separation (right axis), while the bottom frame shows reactive bond lengths throughout the trajectory. Inset snapshots illustrate product structures, with PT highlighted in yellow.

[100]. TS imaginary frequency for reaction (1.1) is 169 cm^{-1} with CH_3NH_2 and 140 cm^{-1} with CD_3NH_2. Consequently, the Wigner tunneling factor [101], calculated as $[1 + \frac{1}{24}(\frac{h\upsilon}{k_B T})^2]$, is 1.03 for CH_3NH_2 and 1.02 for CD_3NH_2, indicating that tunneling can be neglected.

As implied by the trajectory results, the $[9MG + H_{N7}]^+ \cdots {}^\bullet CH_2NH_2$ complex may ultimately rearrange to form various DPCs. These possibilities are explored in Scheme 2A, of which the conversion to $8\text{-}CH_2NH_2[9MG + H_{N7}]^{\bullet +}$ is the most appreciable. That is, k is 8×10^8 s^{-1} at $E_{CM} = 0.05$ eV and increases to 3×10^9 s^{-1} at 0.3 eV. It indicates that crosslinking following methyl-H abstraction is highly effective.

(2) ***Intermediacy of HA_NH₂***: Probable amine-H abstraction pathways are presented in Scheme 2B and Supplementary Scheme S2. According to DFT calculations, the N7, O6, and N3 of $9MG^{\bullet +}$ all exhibit amine-H abstraction capability, leading

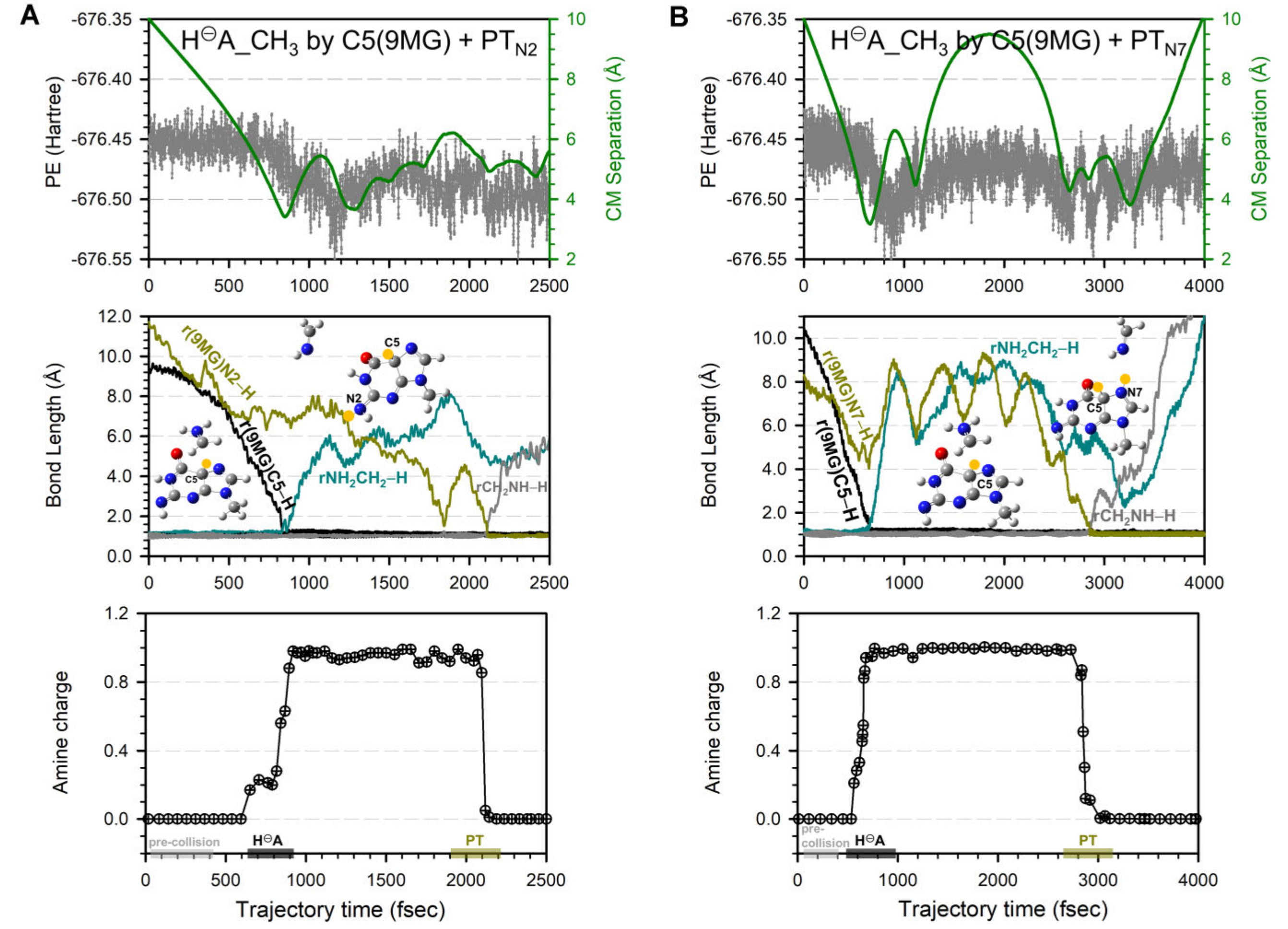

Figure 5. Trajectories for sequential hydride abstraction and PT of $[9MG - H]^+ + CH_3NH_2$ simulated at $E_{CM} = 0.05$ eV, leading to the formation of (**A**) $[9MG + H_{C5}]^+ + CH_2NH$ and (**B**) $[9MG - H_{N2} + H_{C5} + H_{N7}]^+ + CH_2NH$. Each top frame depicts the changes of potential energy (left axis) and center-of-mass reactant/product separation (right axis), the middle frame shows reactive bond lengths, and the bottom frame shows the charge of the amine moiety throughout the trajectory. Inset snapshots illustrate product structures, with $H^{\ominus}A$ and PT highlighted in yellow.

to the formation of a product-like complex and/or separated products as listed in reactions (2.1–2.3). Note that the electronic energy for the H-abstraction TS in reactions (1.2) and (2.1–2.2) is only slightly higher than that of the corresponding product-like complex. Since the TS imaginary frequency is excluded in the thermal correction to the TS energy, the enthalpy of the TS falls below that of the complex.

$$9MG^{\bullet+} + CH_3NH_2 \rightarrow$$

$$[9MG + H_{N7}]^+ \cdots {}^{\bullet}NHCH_3 \quad \Delta H = -0.79\,\text{eV},\ TS = -0.84\,\text{eV} \rightarrow [9MG + H_{N7}]^+ + {}^{\bullet}NHCH_3 \quad \Delta H = 0.14\,\text{eV} \tag{2.1}$$

$$[9MG + H_{O6}]^+ \cdots {}^{\bullet}NHCH_3 \quad \Delta H = -0.21\,\text{eV},\ TS = -0.27\,\text{eV} \rightarrow [9MG + H_{O6}]^+ + {}^{\bullet}NHCH_3 \quad \Delta H = 0.47\,\text{eV} \tag{2.2}$$

$$[9MG + H_{N3}]^+ \cdots {}^{\bullet}NHCH_3 \quad \Delta H = 0.03\,\text{eV},\ TS = 0.31\,\text{eV} \rightarrow [9MG + H_{N3}]^+ + {}^{\bullet}NHCH_3 \quad \Delta H = 0.95\,\text{eV} \tag{2.3}$$

Consistent with the trajectory results, the DFT calculations reveal that only H abstraction by N7, i.e. reaction (2.1), matches the experimental HA_NH_2 threshold (Fig. 1D), confirming its relevance. The TS has an imaginary frequency of 857 cm^{-1} and a Wigner tunneling factor of 1.7, indicating significant H tunneling.

Scheme 2B also illustrates the covalent addition of ${}^{\bullet}NHCH_3$ to $[9MG + H_{N7}]^+$ within the product-like complex $[9MG + H_{N7}]^+ \cdots {}^{\bullet}NHCH_3$. Most addition pathways involve a high barrier and/or yield an endothermic product. Only the formation of $8\text{-}NHCH_3[9MG + H_{N7}]^{\bullet+}$ exhibits exothermicity (−1.09 eV) and a near-thermal barrier (0.02 eV), making it a likely contributor to crosslinking.

Our results highlight the critical role of N7-mediated methyl- and amine-H abstraction in DPC formation. This is supported by the observed reduction of DPCs in N7-capped guanosine [102]. Since methyl-H abstraction dominates over amine-H abstraction at low energies, it is more pertinent to DPCs.

(3) ***C2- and C8-addition***: The addition of CH_3NH_2 to the guanine C2 and C8 was calculated in reactions (3.1–3.2) and illustrated in Scheme 2C and D. The C8-addition represents a previously proposed mechanism for $G^{\bullet+}$-induced DPCs

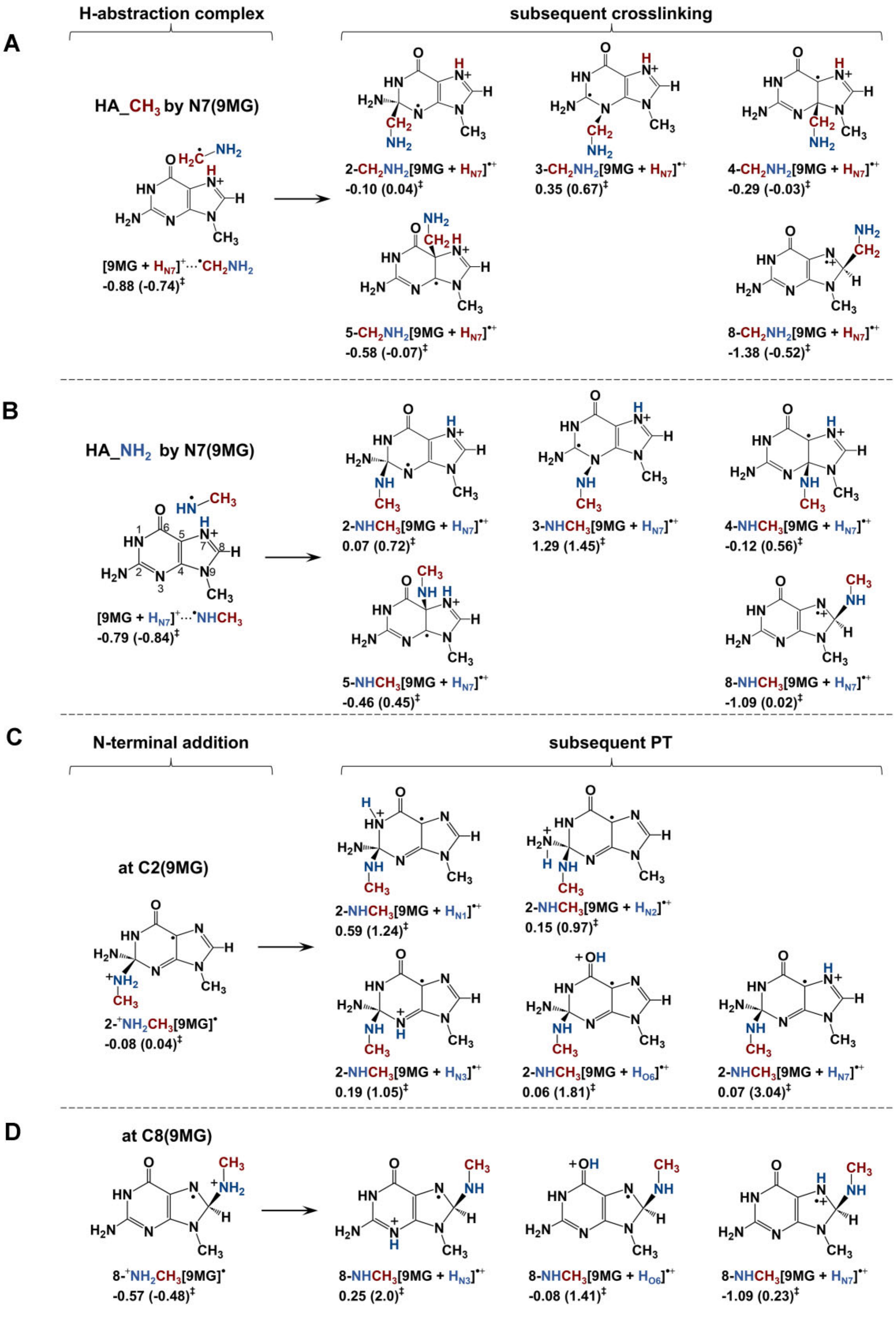

Scheme 2. Most probable reaction pathways for $9MG^{\bullet+}$ + CH_3NH_2 and subsequent crosslinking. Reaction enthalpies (eV) and activation barriers (in parentheses) were calculated at ωB97XD/6-31+G(d,p).

[28–36]. While the resulting adducts may undergo proton transfer to form tautomers [48], all tautomerization processes require substantial barriers and can be disregarded at low energies.

$$9\mathrm{MG}^{\bullet+} + \mathrm{CH_3NH_2} \rightarrow$$

$$2{-}^{+}\mathrm{NH_2CH_3}[9\mathrm{MG}]^{\bullet} \quad \Delta\mathrm{H} = -0.08\,\mathrm{eV},\,\mathrm{TS} = -0.04\,\mathrm{eV} \tag{3.1}$$

$$8{-}^{+}\mathrm{NH_2CH_3}[9\mathrm{MG}]^{\bullet} \quad \Delta\mathrm{H} = -0.57\,\mathrm{eV},\,\mathrm{TS} = -0.48\,\mathrm{eV} \tag{3.2}$$

[9MG – H]$^+$ enhances DPCs via combination of direct addition, and abstraction of H and H$^{\ominus}$

(1) ***N2-, C5-, C8-, and N3-addition***: Trajectory-predicted N2-, C5-, and C8-addition pathways were calculated in Scheme 3A–C and reactions (4.1–4.3), showcasing both primary adducts and downstream proton tautomerization products. The DFT calculations also reveal an exothermic N3 adduct, as presented in Scheme 3D and reaction (4.4). Additionally, probable O6- and N7-adducts for [9MG – H$_{\mathrm{N2}}$]$^+$:NH$_2$CH$_3$ were explored in reactions (4.5–4.6) and Supplementary Scheme S3. However, both reactions involve activation barriers above reactants and are likely relevant only at high energies.

$$[9\mathrm{MG} - \mathrm{H_{N2}}]^{+} + \mathrm{CH_3NH_2} \rightarrow$$

$$2{-}^{+}\mathrm{NH_2CH_3}[9\mathrm{MG} - \mathrm{H_{N2}}] \quad \Delta\mathrm{H} = -1.83\,\mathrm{eV} \rightarrow 2{-}\mathrm{NHCH_3}[9\mathrm{MG} - \mathrm{H_{N2}} + \mathrm{H_{N3}}]^{+} \quad \Delta\mathrm{H} = -2.40\,\mathrm{eV},\,\mathrm{TS} = -1.86\,\mathrm{eV} \tag{4.1}$$

$$5{-}^{+}\mathrm{NH_2CH_3}[9\mathrm{MG} - \mathrm{H_{N2}}] \quad \Delta\mathrm{H} = -1.80\,\mathrm{eV} \tag{4.2}$$

$$8{-}^{+}\mathrm{NH_2CH_3}[9\mathrm{MG} - \mathrm{H_{N2}}] \quad \Delta\mathrm{H} = -1.67\,\mathrm{eV} \tag{4.3}$$

$$3{-}^{+}\mathrm{NH_2CH_3}[9\mathrm{MG} - \mathrm{H_{N2}}] \quad \Delta\mathrm{H} = -0.62\,\mathrm{eV},\,\mathrm{TS} = -0.36\,\mathrm{eV} \tag{4.4}$$

$$6{-}^{+}\mathrm{NH_2CH_3}[9\mathrm{MG} - \mathrm{H_{N2}}] \quad \Delta\mathrm{H} = 0.10\,\mathrm{eV},\,\mathrm{TS} = 0.77\,\mathrm{eV} \tag{4.5}$$

$$7{-}\mathrm{NHCH_3}[9\mathrm{MG} - \mathrm{H_{N2}} + \mathrm{H_{O6}}]^{+} \quad \Delta\mathrm{H} = -1.48\,\mathrm{eV},\,\mathrm{TS} = 0.34\,\mathrm{eV} \tag{4.6}$$

As shown in the trajectories, primary adducts can undergo proton tautomerization. For example, 2-$^+$NH$_2$CH$_3$[9MG – H$_{\mathrm{N2}}$] overwhelmingly converts to 2-NHCH$_3$[9MG – H$_{\mathrm{N2}}$ + H$_{\mathrm{N3}}$]$^+$ in reaction (4.1), with a rate constant of 10^{12} s^{-1} at $E_{\mathrm{CM}} = 0.05$–0.3 eV. This tautomerization occurs within 350 fsec in the trajectory (Fig. 4A). As a result, 2-NHCH$_3$[9MG – H$_{\mathrm{N2}}$ + H$_{\mathrm{N3}}$]$^+$ emerges as the most stable C2-adduct.

(2) ***Methyl hydride abstraction enhances DPCs***: The sequential "methyl hydride abstraction + PT" occurs not only via reaction (5.1) as predicted by the trajectories, but also via reactions (5.2–5.3) as suggested by the DFT calculations, all of which are summarized in Supplementary Scheme S4.

$$[9\mathrm{MG} - \mathrm{H_{N2}}]^{+} + \mathrm{CH_3NH_2} \rightarrow$$

$$\begin{aligned}&[9\mathrm{MG} - \mathrm{H_{N2}} + \mathrm{H_{C5}}]\cdots\mathrm{CH_2}^{+}\mathrm{NH_2} \quad \Delta\mathrm{H} = -2.39\,\mathrm{eV},\,\mathrm{TS} = -0.47\,\mathrm{eV} \rightarrow [9\mathrm{MG} + \mathrm{H_{C5}}]^{+} \text{ or } [9\mathrm{MG} - \mathrm{H_{N2}} + \mathrm{H_{C5}} + \mathrm{H_{N7}}]^{+}\\ &\qquad + \mathrm{CH_2NH} \quad \Delta\mathrm{H} = -1.83/-1.18\,\mathrm{eV}\end{aligned} \tag{5.1}$$

$$\begin{aligned}&[9\mathrm{MG} - \mathrm{H_{N2}} + \mathrm{H_{O6}}]\cdots\mathrm{CH_2}^{+}\mathrm{NH_2} \quad \Delta\mathrm{H} = -2.30\,\mathrm{eV},\,\mathrm{TS} = 0.32\,\mathrm{eV} \rightarrow [9\mathrm{MG} - \mathrm{H_{N2}} + \mathrm{H_{O6}} + \mathrm{H_{N7}}]^{+} + \mathrm{CH_2NH}\\ &\qquad \Delta\mathrm{H} = -1.19\,\mathrm{eV}\end{aligned} \tag{5.2}$$

$$\begin{aligned}&[9\mathrm{MG} - \mathrm{H_{N2}} + \mathrm{H_{N7}}]\cdots\mathrm{CH_2}^{+}\mathrm{NH_2} \quad \Delta\mathrm{H} = -2.30\,\mathrm{eV},\,\mathrm{TS} = 0.18\,\mathrm{eV} \rightarrow [9\mathrm{MG} - \mathrm{H_{N2}} + \mathrm{H_{O6}} + \mathrm{H_{N7}}]^{+} + \mathrm{CH_2NH}\\ &\qquad \Delta\mathrm{H} = -1.19\,\mathrm{eV}\end{aligned} \tag{5.3}$$

$$9\mathrm{MG}\cdots{}^{+}\mathrm{NH_2CH_2} \quad \Delta\mathrm{H} = -3.96\,\mathrm{eV},\,\mathrm{TS} = -0.40\,\mathrm{eV} \tag{5.4}$$

$$[9\mathrm{MG} - \mathrm{H_{N2}} + \mathrm{H_{N3}}]\cdots{}^{+}\mathrm{NH_2CH_2} \quad \Delta\mathrm{H} = -3.20\,\mathrm{eV},\,\mathrm{TS} = -0.38\,\mathrm{eV} \tag{5.5}$$

We are more interested in exploring stand-alone H$^{\ominus}$A without subsequent PT, as these products may contribute to DPCs. Reactions (5.4–5.5) present the products formed from methyl hydride abstraction by the N2 and N3 of [9MG – H]$^+$. Experimentally, no $^+$NH$_2$CD$_2$ product ions were detected, suggesting that these hydride abstraction products, once generated, undergo further reactions leading to DPC formation, as depicted in Scheme 4. Based on density of states calculations, the two dominant adducts are 5-CH$_2$NH$_2$[9MG]$^+$ and 8-CH$_2$NH$_2$[9MG]$^+$, each contributing ~50% to the adduct population. A significant KIE is expected, with $k_{\mathrm{H}}/k_{\mathrm{D}}$ ratios of 4.5–5.0 for reaction (5.4) and 2.3–4.0 for reaction (5.5) at $E_{\mathrm{CM}} = 0.05$–0.3 eV. The Wigner tunneling factors are 1.32 (for CH$_3$NH$_2$) and 1.48 (CD$_3$NH$_2$) for reaction (5.4), and 1.83 (CH$_3$NH$_2$) and 2.33 (CD$_3$NH$_2$) for reaction (5.5). It is noteworthy that H$^{\ominus}$A may initiate at the amine group; however, the resulting CH$_3$NH$^+$ product rapidly rearranges to CH$_2{}^+$NH$_2$.

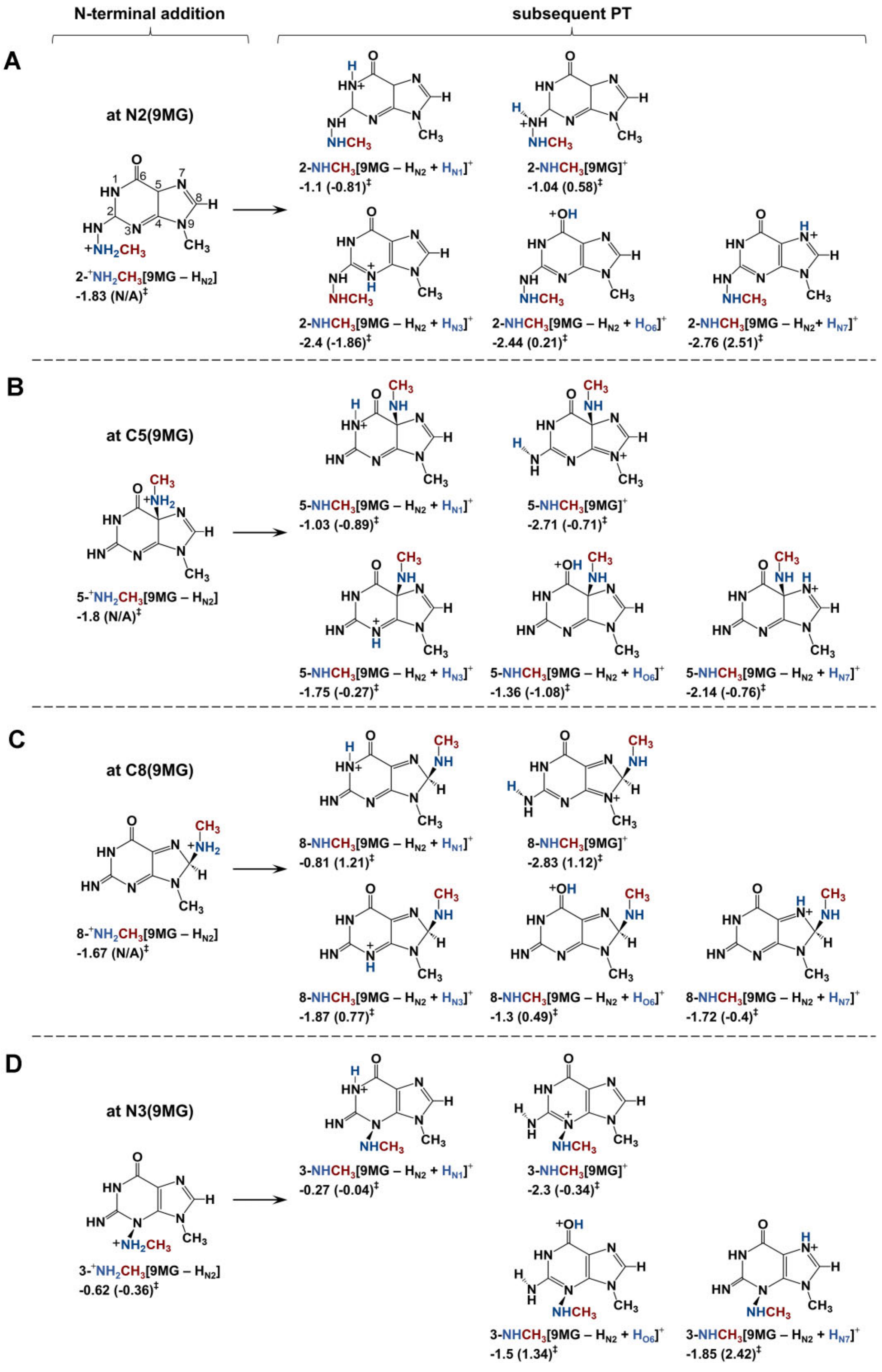

Scheme 3. Barrierless direct addition pathways for [9MG – H]$^+$ + CH_3NH_2 and subsequent proton tautomerization. Reaction enthalpies (eV) and activation barriers (in parentheses) were calculated at ωB97XD/6-31+G(d,p).

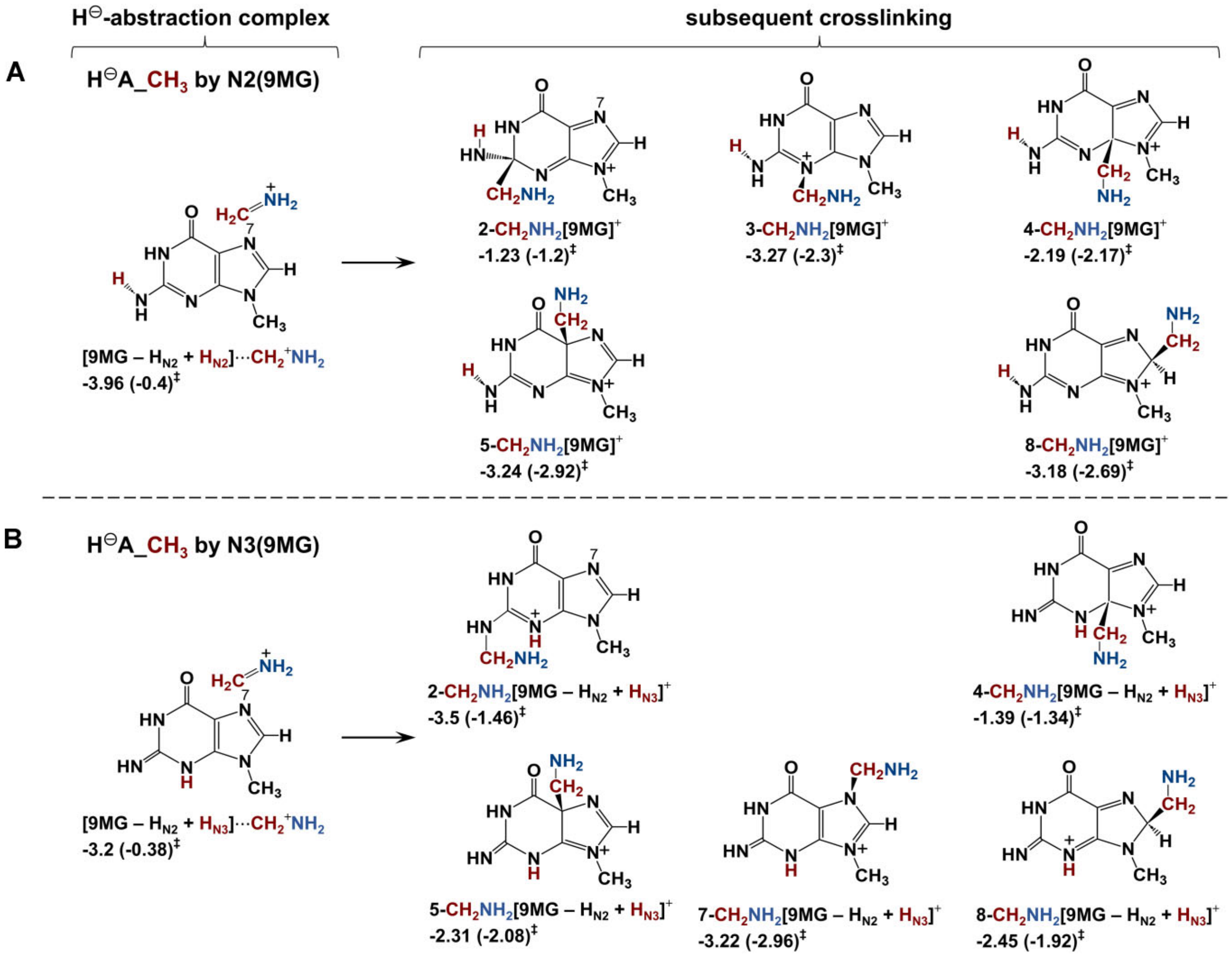

Scheme 4. Methyl hydride abstraction for $[9MG - H]^+$ + CH_3NH_2 and subsequent crosslinking. Reaction enthalpies (eV) and activation barriers (in parentheses) were calculated at ωB97XD/6-31+G(d,p).

(3) ***H abstraction and combination of radical product pairs***: To facilitate a point-to-point comparison with the reaction pathways of $9MG^{\bullet+}$ + CH_3NH_2, hydrogen abstraction for $[9MG - H]^+$ + CH_3NH_2 was evaluated using open-shell DFT calculations. Only one methyl-H abstraction pathway was identified, as shown in reaction (6.1) and Scheme 5A. On the other hand, reactions (6.2–6.5) and Scheme 5B–E illustrate a total of four probable pathways for amine-H abstraction. The H-abstraction reactions yield radical product pairs, $^{1,OS}[9MG^{\bullet+}(\uparrow)\cdots(\downarrow)^{\bullet}CH_2NH_2]$ and $^{1,OS}[9MG^{\bullet+}(\uparrow)\cdots(\downarrow)^{\bullet}NHCH_3]$, which introduce spin contamination in single-reference DFT calculations. To resolve this issue, approximate spin projection [80–83] was applied for the spin purification of reaction electronic energies.

$$[9MG - H_{N2}]^+ + CH_3NH_2 \rightarrow$$

$$[9MG - H_{N2} + H_{O6}]^{\bullet+}\cdots{}^{\bullet}CH_2NH_2 \quad \Delta H = -0.97\,eV,\ TS = -1.00\,eV \rightarrow [9MG - H_{N2} + H_{O6}]^{\bullet+} + {}^{\bullet}CH_2NH_2 \quad \Delta H = -0.04\,eV \tag{6.1}$$

$$9MG^{\bullet+}\cdots{}^{\bullet}NHCH_3 \quad \Delta H = -1.24\,eV,\ TS = -0.51\,eV \rightarrow 9MG^{\bullet+} + {}^{\bullet}NHCH_3 \quad \Delta H = -0.37\,eV \tag{6.2}$$

$$[9MG - H_{N2} + H_{N3}]^{\bullet+}\cdots{}^{\bullet}NHCH_3 \quad \Delta H = -0.27\,eV,\ TS = -0.20\,eV \rightarrow [9MG - H_{N2} + H_{N3}]^{\bullet+} + {}^{\bullet}NHCH_3 \quad \Delta H = 0.74\,eV \tag{6.3}$$

$$[9MG - H_{N2} + H_{O6}]^{\bullet+}\cdots{}^{\bullet}NHCH_3 \quad \Delta H = -0.71\,eV,\ TS = -0.78\,eV \rightarrow [9MG - H_{N2} + H_{O6}]^{\bullet+} + {}^{\bullet}NHCH_3 \quad \Delta H = 0.25\,eV \tag{6.4}$$

$$[9MG - H_{N2} + H_{N7}]^{\bullet+}\cdots{}^{\bullet}NHCH_3 \quad \Delta H = -0.70\,eV,\ TS = -0.77\,eV \rightarrow [9MG - H_{N2} + H_{N7}]^{\bullet+} + {}^{\bullet}NHCH_3 \quad \Delta H = 0.16\,eV \tag{6.5}$$

The exothermic, barrierless methyl-H abstraction of CH_3NH_2 via reaction (6.1) results in the formation of the major experimental product ion, i.e. d_1-$[9MG - H_{N2} + H_{O6}]^{\bullet+}$ at m/z 166 in Fig. 2A. The significance of methyl-H abstraction is further reflected by the potential combination of $[9MG - H_{N2} + H_{O6}]^{\bullet+}$ with ${}^{\bullet}CH_2NH_2$ to form a DPC, as illustrated in Scheme 5A.

The product-like complex $9MG^{\bullet+}\cdots{}^{\bullet}NHCH_3$, formed in reaction (6.2), is the most favorable outcome of amine-H abstraction. The associated TS has an imaginary frequency of 446 cm^{-1}, indicating negligible tunneling. While $9MG^{\bullet+}\cdots{}^{\bullet}NHCH_3$ may separate into $9MG^{\bullet+}$ + ${}^{\bullet}NHCH_3$, with an asymptote at −0.37 eV, the covalent association of the radical product pair is kinetically

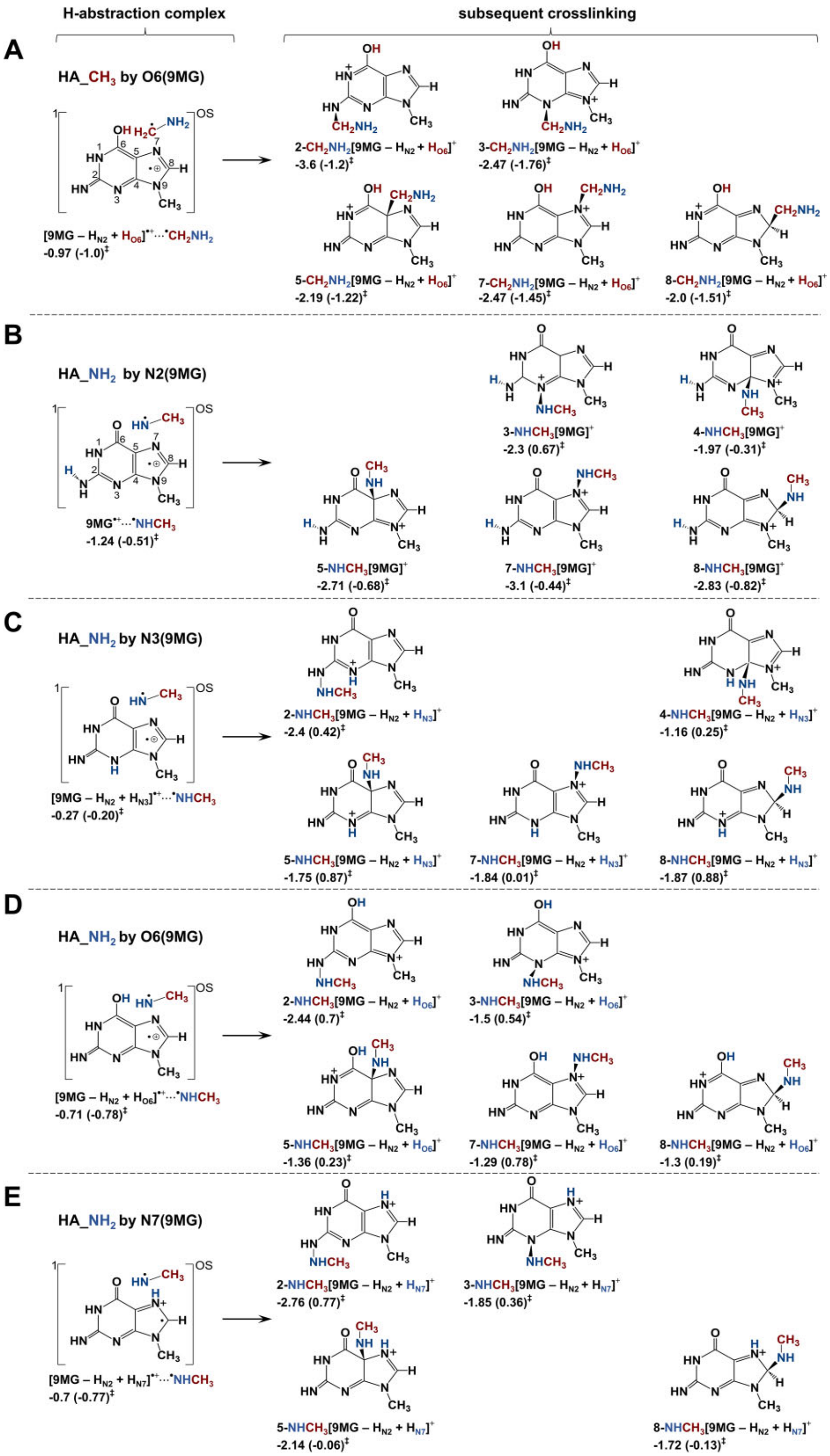

Scheme 5. Amine and methyl hydrogen abstraction for $[9MG – H]^+ + CH_3NH_2$ and subsequent crosslinking. Reaction enthalpies (eV) and activation barriers (in parentheses) were calculated using approximately spin-projected ωB97XD/6-31+G(d,p).

Table 1. The comparison of CH_3NH_2 with $9MG^{\bullet+}$ versus $[9MG - H]^+$

	Thermal energy			High energy (1–2 eV)		
	Yield%	**Mechanism**	**Adducts**	**Yield%**	**Mechanism**	**Adducts**
$9MG^{\bullet+}$	2.8	HA_CH_3 (major) Direct addition	$8\text{-}CH_2NH_2[9MG + H_{N7}]^{\bullet+}$ $X\text{-}NH_2CH_3[9MG]^{\bullet+}$ ($X =$ C2, C8)	0	N/A	None
$[9MG - H]^+$	9.3	Direct addition (major) HA_CH_3	$X\text{-}^+NH_2CH_3[9MG - H_{N2}]$ (major, $X =$ N2, N3, C5, and C8) $X\text{-}CH_2NH_2[9MG - H_{N2} + H_{O6}]^+$ (minor, $X =$ N2, N3, C5, N7, and C8)	1.5	Direct addition	$X\text{-}^+NH_2CH_3[9MG - H_{N2}]$ ($X =$ N2, N3, C5, and C8)

more favorable. This may explain the low intensity of product ions at *m*/*z* 165 in Fig. 2A. Kinetics modeling suggests that $8\text{-}NHCH_3[9MG]^+$ is the dominating adduct (if any) resulting from the combination of amine-H abstraction products.

Comparison of one- versus two-electron oxidation-mediated crosslinking

Table 1 highlights distinct features and differences in crosslinking mediated by $9MG^{\bullet+}$ versus $[9MG - H]^+$. Reactions were examined over a wide range of energy, and the lowest reaction energy was selected to match the thermal energy of reactants at room temperature, ensuring biological relevance. The crosslinking yield for $9MG^{\bullet+}$ is <3% at thermal energy and becomes negligible at energies >0.3 eV. In contrast, the crosslinking yield for $[9MG - H]^+$ exceeds 9% at thermal energy and remains significant (1.5%) even at high energies.

The large difference in DPC yields and their energy dependence can be attributed to distinct crosslinking mechanisms. For $9MG^{\bullet+}$, crosslinking is mediated by direct addition and, to a greater extent, by covalent combination of the product pair $[9MG + H]^+\cdots{}^\bullet CH_2NH_2$ resulting from methyl-H abstraction. As the formation efficiency and lifetime of complexes are both suppressed by energy, it is rational that crosslinking diminishes as reaction energy increases. In contrast, crosslinking for $[9MG - H]^+$ is predominant driven by direct addition between reactants. Since the addition pathways for $[9MG - H]^+ + CH_3NH_2$ are exothermic and barrierless, reaction yield at high energies is mainly influenced by dynamics factors such as reaction orientations and thus becomes nearly constant. Methyl-H abstraction assists in crosslinking for $[9MG - H]^+$ only at low energies. Following divergent reaction mechanisms, the crosslinking for $9MG^{\bullet+}$ is primarily dominated by a $8\text{-}CH_2NH_2[9MG + H_{N7}]^{\bullet+}$ adduct, whereas the crosslinking for $[9MG - H]^+$ leads to $X\text{-}^+NH_2CH_3[9MG - H_{N2}]$ ($X =$ N2, N3, C5, and C8) and their proton tautomers, with a minor contribution from $X\text{-}CH_2NH_2[9MG - H_{N2} + H_{O6}]^+$ ($X =$ N2, N3, C5, N7, and C8) at low energies.

Conclusions

This study presents a synergistic experimental and computational investigation into the reactions of methylamine with $9MG^{\bullet+}$ and $[9MG - H]^+$, designed to mimic and elucidate DNA–protein crosslinks induced by one- and two-electron oxidized guanosine nucleosides. While both singly and doubly oxidized guanosine species form under oxidative stress, their roles in the formation of DPCs remain elusive because of the difficulties in separating and characterizing these short-lived intermediates in solution-phase systems. This combined gas-phase experimental and theoretical work has, for the first time, uncovered new and distinct crosslinking mechanisms, products, yields, and reaction energy dependence for the two species. Crosslinking between $9MG^{\bullet+}$ and methylamine primarily initiates with hydrogen abstraction from methylamine by $9MG^{\bullet+}$, followed by the addition of the nascent ${}^\bullet CH_2NH_2$ radical to protonated $[9MG + H]^+$. Another pathway involves the addition of methylamine to the C2 and C8 of $9MG^{\bullet+}$, as previously reported. Despite being exothermic and barrierless, crosslinking for $9MG^{\bullet+}$ occurs only at low reaction energies and exhibits a low yield. In contrast, $[9MG - H]^+$ predominantly undergoes direct addition with the N-terminal of methyl amine, followed by proton tautomerization of the product. The reaction operates efficiently across a wide range of energies and achieves three times the crosslinking yield of $9MG^{\bullet+}$. Hydrogen abstraction from methylamine also contributes to the crosslinking of $[9MG - H]^+$. This work has identified key intermediates and adduct structures involved in DPC formation and, particularly, underscored the critical role of two-electron nucleoside oxidation in driving these processes. The gas-phase experimental and computational results not only offer guidance for the experimental exploration of various structures in solution-phase DNA–protein coupling within biochemical systems but also serve as a foundation for understanding downstream oxidative DNA damage resulting from primary DPC products.

Acknowledgements

This work was supported by the National Science Foundation (Grant No. CHE 2350109). M.M.M. acknowledges the CUNY Mina Rees Dissertation Fellowship.

Author Contributions: M.M.M.: Data curation, Formal analysis, Investigation, Methodology, Validation, Visualization, and Manuscript writing. J.B.: Data curation, Formal analysis, Investigation, Methodology, Software, and Validation. V.L.: Data curation, Formal analysis, and Investigation. M.T.: Data curation, Formal analysis, Investigation, and Software. J.L.: Conceptualization, Data curation, Formal analysis, Funding acquisition, Investigation, Methodology, Project administration, Resources, Software, Supervision, Validation, and Manuscript writing and revision.

Supplementary data

Supplementary data is available at NAR online.

Conflict of interest

None declared.

Funding

National Science Foundation (Grant No. CHE 2350109). Funding to pay the Open Access publication charges for this article was provided by National Science Foundation.

Data availability

All data are incorporated into the article and its online supplementary material.

References

1. Echols H. Multiple DNA–protein interactions governing high-precision DNA transactions. *Science* 1986;**233**:1050–6. https://doi.org/10.1126/science.2943018
2. Vigneault F, Guérin SL. Regulation of gene expression: probing DNA–protein interactions *in vivo* and *in vitro*. *Expert Rev Proteomics* 2005;**2**:705–18. https://doi.org/10.1586/14789450.2.5.705
3. Kojima Y, Machida YJ. DNA–protein crosslinks from environmental exposure: mechanisms of formation and repair. *Environ Mol Mutagen* 2020;**61**:716–29. https://doi.org/10.1002/em.22381
4. Tretyakova NY, Groehler A, Ji S. DNA–protein cross-links: formation, structural identities, and biological outcomes. *Acc Chem Res* 2015;**48**:1631–44. https://doi.org/10.1021/acs.accounts.5b00056
5. Ide H, Nakano T, Salem AMH *et al.* DNA–protein cross-links: formidable challenges to maintaining genome integrity. *DNA Repair (Amst)* 2018;**71**:190–7. https://doi.org/10.1016/j.dnarep.2018.08.024
6. Duxin JP, Dewar JM, Yardimci H *et al.* Repair of a DNA–protein crosslink by replication-coupled proteolysis. *Cell* 2014;**159**:346–57. https://doi.org/10.1016/j.cell.2014.09.024
7. Margolis SA, Coxon B, Gajewski E *et al.* Structure of a hydroxyl radical induced cross-link of thymine and tyrosine. *Biochemistry* 1988;**27**:6353–9. https://doi.org/10.1021/bi00417a024
8. Solivio MJ, Nemera DB, Sallans L *et al.* Biologically relevant oxidants cause bound proteins to readily oxidatively cross-link at guanine. *Chem Res Toxicol* 2012;**25**:326–36. https://doi.org/10.1021/tx200376e
9. Steenken S, Jovanovic SV. How easily oxidizable is DNA? One-electron reduction potentials of adenosine and guanosine radicals in aqueous solution. *J Am Chem Soc* 1997;**119**:617–8. https://doi.org/10.1021/ja962255b
10. Burrows CJ, Muller JG. Oxidative nucleobase modifications leading to strand scission. *Chem Rev* 1998;**98**:1109–52. https://doi.org/10.1021/cr960421s
11. Caruso T, Carotenuto M, Vasca E *et al.* Direct experimental observation of the effect of the base pairing on the oxidation potential of guanine. *J Am Chem Soc* 2005;**127**:15040–1. https://doi.org/10.1021/ja055130s
12. Crespo-Hernández CE, Close DM, Gorb L *et al.* Determination of redox potentials for the Watson–Crick base pairs, DNA nucleosides, and relevant nucleoside analogs. *J Phys Chem B* 2007;**111**:5386–95. https://doi.org/10.1021/jp0684224
13. Candeias LP, Steenken S. Ionization of purine nucleosides and nucleotides and their components by 193-nm laser photolysis in aqueous solution: model studies for oxidative damage of DNA. *J Am Chem Soc* 1992;**114**:699–704. https://doi.org/10.1021/ja00028a043
14. Candeias LP, Steenken S. Structure and acid-base properties of one-electron-oxidized deoxyguanosine, guanosine, and 1-methylguanosine. *J Am Chem Soc* 1989;**111**:1094–9. https://doi.org/10.1021/ja00185a046
15. Stemp EDA, Barton JK. Electron transfer between metal complexes bound to DNA: is DNA a wire? *Met Ions Biol Syst* 1996;**33**:325–65.
16. Thorp HH. Cutting out the middleman: DNA biosensors based on electrochemical oxidation. *Trends Biotechnol* 1998;**16**:117–21. https://doi.org/10.1016/S0167-7799(97)01162-1
17. Kasai H, Yamaizumi Z, Berger M *et al.* Photosensitized formation of 7,8-dihydro-8-oxo-2′-deoxyguanosine (8-hydroxy-2′-deoxyguanosine) in DNA by riboflavin: a non singlet oxygen-mediated reaction. *J Am Chem Soc* 1992;**114**:9692–4. https://doi.org/10.1021/ja00050a078
18. Lewis FD, Liu X, Liu J *et al.* Direct measurement of hole transport dynamics in DNA. *Nature* 2000;**406**:51–3. https://doi.org/10.1038/35017524
19. Steenken S. Purine bases, nucleosides, and nucleotides: aqueous solution redox chemistry and transformation reactions of their radical cations and e^- and OH adducts. *Chem Rev* 1989;**89**:503–20. https://doi.org/10.1021/cr00093a003
20. Cadet J, Douki T, Ravanat J-L. Oxidatively generated base damage to cellular DNA. *Free Radic Biol Med* 2010;**49**:9–21.
21. Cadet J, Wagner JR. DNA base damage by reactive oxygen species, oxidizing agents, and UV radiation. *Cold Spring Harb Perspect Biol* 2013;**5**:a012559. https://doi.org/10.1101/cshperspect.a012559
22. Neeley WL, Essigmann JM. Mechanisms of formation, genotoxicity, and mutation of guanine oxidation products. *Chem Res Toxicol* 2006;**19**:491–505. https://doi.org/10.1021/tx0600043
23. Fleming AM, Burrows CJ. Formation and processing of DNA damage substrates for the hNEIL enzymes. *Free Radic Biol Med* 2017;**107**:35–52.

24. Becker D, Sevilla MD. In: Lett JT, Sinclair WK (eds.), *Advances in Radiation Biology*. San Diego, CA: Academic Press, Inc., Vol. **17**, 1993, 121–80.
25. Sevilla MD, Becker D, Kumar A *et al.* Gamma and ion-beam irradiation of DNA: free radical mechanisms, electron effects, and radiation chemical track structure. *Radiat Phys Chem* 2016;**128**:60–74. https://doi.org/10.1016/j.radphyschem.2016.04.022
26. Cullis PM, Malone ME, Merson-Davies LA. Guanine radical cations are precursors of 7,8-dihydro-8-oxo-2′-deoxyguanosine but are not precursors of immediate strand breaks in DNA. *J Am Chem Soc* 1996;**118**:2775–81. https://doi.org/10.1021/ja9536025
27. Fleming AM, Burrows CJ. 8-oxo-7,8-dihydroguanine, friend and foe: epigenetic-like regulator versus initiator of mutagenesis. *DNA Repair (Amst)* 2017;**56**:75–83. https://doi.org/10.1016/j.dnarep.2017.06.009
28. Morin B, Cadet J. Type I benzophenone-mediated nucleophilic reaction of 5′-amino-2′,5′-dideoxyguanosine. A model system for the investigation of photosensitized formation of DNA–protein cross-links. *Chem Res Toxicol* 1995;**8**:792–9. https://doi.org/10.1021/tx00047a020
29. Morin B, Cadet J. Chemical aspects of the benzophenone-photosensitized formation of two lysine-2′-deoxyguanosine cross-links. *J Am Chem Soc* 1995;**117**:12408–15. https://doi.org/10.1021/ja00155a005
30. Perrier S, Hau J, Gasparutto D *et al.* Characterization of lysine-guanine cross-links upon one-electron oxidation of a guanine-containing oligonucleotide in the presence of a trilysine peptide. *J Am Chem Soc* 2006;**128**:5703–10. https://doi.org/10.1021/ja057656i
31. Silerme S, Bobyk L, Taverna-Porro M *et al.* DNA-polyamine cross-links generated upon one electron oxidation of DNA. *Chem Res Toxicol* 2014;**27**:1011–8. https://doi.org/10.1021/tx500063d
32. Xu X, Muller JG, Ye Y *et al.* DNA–protein cross-links between guanine and lysine depend on the mechanism of oxidation for formation of C5 vs C8 guanosine adducts. *J Am Chem Soc* 2008;**130**:703–9. https://doi.org/10.1021/ja077102a
33. Fleming AM, Armentrout EI, Zhu J *et al.* Spirodi(iminohydantoin) products from oxidation of 2′-deoxyguanosine in the presence of NH_4Cl in nucleoside and oligodeoxynucleotide contexts. *J Org Chem* 2015;**80**:711–21. https://doi.org/10.1021/jo502665p
34. Nguyen KL, Steryo M, Kurbanyan K *et al.* DNA–protein cross-linking from oxidation of guanine via the flash-quench technique. *J Am Chem Soc* 2000;**122**:3585–94. https://doi.org/10.1021/ja993502p
35. Kurbanyan K, Nguyen KL, To P *et al.* DNA–protein cross-linking via guanine oxidation: dependence upon protein and photosensitizer. *Biochemistry* 2003;**42**:10269–81. https://doi.org/10.1021/bi020713p
36. Madison AL, Perez ZA, To P *et al.* Dependence of DNA–protein cross-linking via guanine oxidation upon local DNA sequence as studied by restriction endonuclease inhibition. *Biochemistry* 2012;**51**:362–9. https://doi.org/10.1021/bi201087q
37. Ye Y, Muller JG, Luo W *et al.* Formation of ^{13}C-, ^{15}N-, and ^{18}O-labeled guanidinohydantoin from guanosine oxidation with singlet oxygen. Implications for structure and mechanism. *J Am Chem Soc* 2003;**125**:13926–7. https://doi.org/10.1021/ja0378660
38. Munk BH, Burrows CJ, Schlegel HB. An exploration of mechanisms for the transformation of 8-oxoguanine to guanidinohydantoin and spiroiminodihydantoin by density functional theory. *J Am Chem Soc* 2008;**130**:5245–56. https://doi.org/10.1021/ja7104448
39. Hickerson RP, Chepanoske CL, Williams SD *et al.* Mechanism-based DNA–protein cross-linking of MutY via oxidation of 8-oxoguanosine. *J Am Chem Soc* 1999;**121**:9901–2. https://doi.org/10.1021/ja9923484
40. Johansen ME, Muller JG, Xu X *et al.* Oxidatively induced DNA−protein cross-linking between single-stranded binding protein and oligodeoxynucleotides containing 8-oxo-7,8-dihydro-2′-deoxyguanosine. *Biochemistry* 2005;**44**:5660–71. https://doi.org/10.1021/bi047580n
41. Hosford ME, Muller JG, Burrows CJ. Spermine participates in oxidative damage of guanosine and 8-oxoguanosine leading to deoxyribosylurea formation. *J Am Chem Soc* 2004;**126**:9540–1. https://doi.org/10.1021/ja047981q
42. Xu X, Fleming AM, Muller JG *et al.* Formation of tricyclic [4.3.3.0] adducts between 8-oxoguanosine and tyrosine under conditions of oxidative DNA–protein cross-linking. *J Am Chem Soc* 2008;**130**:10080–1. https://doi.org/10.1021/ja803896d
43. Sun Y, Tsai M, Zhou W *et al.* Reaction kinetics, product branching, and potential energy surfaces of $^1O_2$-induced 9-methylguanine–lysine cross-linking: a combined mass spectrometry, spectroscopy, and computational study. *J Phys Chem B* 2019;**123**:10410–23. https://doi.org/10.1021/acs.jpcb.9b08796
44. Mee LK, Adelstein SJ. Predominance of core histones in formation of DNA–protein crosslinks in gamma-irradiated chromatin. *Proc Natl Acad Sci USA* 1981;**78**:2194–8. https://doi.org/10.1073/pnas.78.4.2194
45. Uvaydov Y, Geacintov NE, Shafirovich V. Generation of guanine-amino acid cross-links by a free radical combination mechanism. *Phys Chem Chem Phys* 2014;**16**:11729–36. https://doi.org/10.1039/C4CP00675E
46. Thapa B, Munk BH, Burrows CJ *et al.* Computational study of the radical mediated mechanism of the formation of C8, C5, and C4 guanine:lysine adducts in the presence of the benzophenone photosensitizer. *Chem Res Toxicol* 2016;**29**:1396–409. https://doi.org/10.1021/acs.chemrestox.6b00057
47. Thapa B, Munk BH, Burrows CJ *et al.* Computational study of oxidation of guanine by singlet oxygen ($^1\Delta_g$) and formation of guanine:lysine cross-links. *Chemistry* 2017;**23**:5804–13. https://doi.org/10.1002/chem.201700231
48. Thapa B, Hebert SP, Munk BH *et al.* Computational study of the formation of C8, C5, and C4 guanine:lysine adducts via oxidation of guanine by sulfate radical anion. *J Phys Chem A* 2019;**123**:5150–63. https://doi.org/10.1021/acs.jpca.9b03598
49. Jena NR, Mishra PC. Interaction of guanine, its anions, and radicals with lysine in different charge states. *J Phys Chem B* 2007;**111**:5418–24. https://doi.org/10.1021/jp0703004
50. Labet V, Morell C, Grand A *et al.* Formation of cross-linked adducts between guanine and thymine mediated by hydroxyl radical and one-electron oxidation: a theoretical study. *Org Biomol Chem* 2008;**6**:3300–5. https://doi.org/10.1039/b805589k
51. Bignon E, Chan C-H, Morell C *et al.* Molecular dynamics insights into polyamine-DNA binding modes: implications for crosslink selectivity. *Chemistry* 2017;**23**:12845–52. https://doi.org/10.1002/chem.201702065
52. Chan C-H, Monari A, Ravanat J-L *et al.* Probing interaction of a trilysine peptide with DNA behind formation of guanine-lysine cross-links: insights from molecular dynamics. *Phys Chem Chem Phys* 2019;**21**:23418–24. https://doi.org/10.1039/C9CP04708E
53. Pratviel G, Meunier B. Guanine oxidation: one- and two-electron reactions. *Chemistry* 2006;**12**:6018–30. https://doi.org/10.1002/chem.200600539
54. Koppang MD, Witek M, Blau J *et al.* Electrochemical oxidation of polyamines at diamond thin-film electrodes. *Anal Chem* 1999;**71**:1188–95. https://doi.org/10.1021/ac980697v
55. Fang Y, Liu J. Reaction of protonated tyrosine with electronically excited singlet molecular oxygen (a$^1\Delta_g$): an experimental and trajectory study. *J Phys Chem A* 2009;**113**:11250–61. https://doi.org/10.1021/jp905978z

56. Sun Y, Tsai M, Moe MM *et al.* Dynamics and multiconfiguration potential energy surface for the singlet O_2 reactions with radical cations of guanine, 9-methylguanine, 2′-deoxyguanosine, and guanosine. *J Phys Chem A* 2021;**125**:1564–76. https://doi.org/10.1021/acs.jpca.1c00095
57. Wee S, O'Hair RAJ, McFadyen WD. Can radical cations of the constituents of nucleic acids be formed in the gas phase using ternary transition metal complexes? *Rapid Commun Mass Spectrom* 2005;**19**:1797–805. https://doi.org/10.1002/rcm.1988
58. Lam AKY, Abrahams BF, Grannas MJ *et al.* Tuning the gas phase redox properties of copper(II) ternary complexes of terpyridines to control the formation of nucleobase radical cations. *Dalton Trans* 2006;5051–61. https://doi.org/10.1039/b609688c
59. Cheng P, Bohme DK. Gas-phase formation of radical cations of monomers and dimers of guanosine by collision-induced dissociation of Cu(II)-guanosine complexes. *J Phys Chem B* 2007;**111**:11075–82. https://doi.org/10.1021/jp071933l
60. Dang A, Liu Y, Tureček F. Uv-vis action spectroscopy of guanine, 9-methylguanine, and guanosine cation radicals in the gas phase. *J Phys Chem A* 2019;**123**:3272–84. https://doi.org/10.1021/acs.jpca.9b01542
61. Armentrout PB. Fundamental of ion-molecule chemistry. *J Anal At Spectrom* 2004;**19**:571–80. https://doi.org/10.1039/B313133E
62. Ervin KM, Armentrout PB. Translational energy dependence of $Ar^+ + XY \rightarrow ArX^+ + Y$ ($XY = H_2, D_2$, HD) from thermal to 30 eV c.m. *J Chem Phys* 1985;**83**:166–89. https://doi.org/10.1063/1.449799
63. Levine RD, Bernstein RB. *Molecular Reaction Dynamics and Chemical Reactivity*. New York: Oxford University Press, 1987.
64. Liu J, van Devener B, Anderson SL. Collision-induced dissociation of formaldehyde cations: the effects of vibrational mode, collision energy, and impact parameter. *J Chem Phys* 2002;**116**:5530–43. https://doi.org/10.1063/1.1457438
65. Chantry PJ. Doppler broadening in beam experiments. *J Chem Phys* 1971;**55**:2746–59. https://doi.org/10.1063/1.1676489
66. Lifshitz C. Kinetic shifts. *Eur J Mass Spectrom (Chichester)* 2002;**8**:85–98. https://doi.org/10.1255/ejms.476
67. Sun Y, Moe MM, Liu J. Mass spectrometry and computational study of collision-induced dissociation of 9-methylguanine-1-methylcytosine base-pair radical cation: intra-base-pair proton transfer and hydrogen transfer, non-statistical dissociation, and reaction with a water ligand. *Phys Chem Chem Phys* 2020;**22**:14875–88. https://doi.org/10.1039/D0CP01788D
68. Sowa-Resat MB, Hintz PA, Anderson SL. Dissociation energies for small carbon cluster ions ($C_{2\text{-}19}{}^+$) measured by collision-induced dissociation. *J Phys Chem* 1995;**99**:10736–41. https://doi.org/10.1021/j100027a010
69. Hu X, Hase WL, Pirraglia T. Vectorization of the general Monte Carlo classical trajectory program venus. *J Comput Chem* 1991;**12**:1014–24. https://doi.org/10.1002/jcc.540120814
70. Hase WL, Bolton K, de Sainte Claire P *et al.* Venus 99: A General Chemical Dynamics Computer Program. Lubbock, TX: Texas Tech University, 1999.
71. Frisch MJ, Trucks GW, Schlegel HB *et al.* Gaussian 16. Rev D.01. Wallingford, CT: Gaussian, Inc., 2016.
72. Bakken V, Millam JM, Schlegel HB. Ab initio classical trajectories on the Born-Oppenheimer surface: updating methods for Hessian-based integrators. *J Chem Phys* 1999;**111**:8773–7. https://doi.org/10.1063/1.480224
73. Chai J-D, Head-Gordon M. Long-range corrected hybrid density functionals with damped atom–atom dispersion corrections. *Phys Chem Chem Phys* 2008;**10**:6615–20. https://doi.org/10.1039/b810189b
74. Kumar A, Pottiboyina V, Sevilla MD. One-electron oxidation of neutral sugar radicals of 2′-deoxyguanosine and 2′-deoxythymidine: a density functional theory (DFT) study. *J Phys Chem B* 2012;**116**:9409–16. https://doi.org/10.1021/jp3059068
75. Kumar A, Sevilla MD. Proton transfer induced SOMO-to-HOMO level switching in one-electron oxidized A-T and G-C base pairs: a density functional theory study. *J Phys Chem B* 2014;**118**:5453–8. https://doi.org/10.1021/jp5028004
76. Sun Y, Zhou W, Moe MM *et al.* Reactions of water with radical cations of guanine, 9-methylguanine, 2′-deoxyguanosine and guanosine: keto-enol isomerization, C8-hydroxylation, and effects of N9-substitution. *Phys Chem Chem Phys* 2018;**20**:27510–22. https://doi.org/10.1039/C8CP05453C
77. Moe MM, Tsai M, Liu J. Singlet oxygen oxidation of the radical cations of 8-oxo-2′-deoxyguanosine and its 9-methyl analogue: dynamics, potential energy surface, and products mediated by C5-O_2-addition. *ChemPlusChem* 2021;**86**:1243–54. https://doi.org/10.1002/cplu.202100238
78. Peslherbe GH, Wang H, Hase WL. Monte Carlo sampling for classical trajectory simulations. *Adv Chem Phys* 1999;**105**:171–201.
79. Aragoni MC, Caltagirone C, Lippolis V *et al.* Diradical character of neutral heteroleptic bis(1,2-dithiolene) metal complexes: case study of [Pd(Me_2timdt)(mnt)] (Me_2timdt = 1,3-dimethyl-2,4,5-trithioxoimidazolidine; mnt^{2-} = 1,2-dicyano-1,2-ethylenedithiolate). *Inorg Chem* 2020;**59**:17385–401. https://doi.org/10.1021/acs.inorgchem.0c02696
80. Yamaguchi K, Jensen F, Dorigo A *et al.* A spin-correction procedure for unrestricted Hartree-Fock and Møller-Plesset wave functions for singlet diradicals and polyradicals. *Chem Phys Lett* 1988;**149**:537–42. https://doi.org/10.1016/0009-2614(88)80378-6
81. Saito T, Nishihara S, Kataoka Y *et al.* Transition state optimization based on approximate spin-projection (AP) method. *Chem Phys Lett* 2009;**483**:168–71. https://doi.org/10.1016/j.cplett.2009.10.055
82. Saito T, Nishihara S, Kataoka Y *et al.* Reinvestigation of the reaction of ethylene and singlet oxygen by the approximate spin projection method. Comparison with multireference coupled-cluster calculations. *J Phys Chem A* 2010;**114**:7967–74. https://doi.org/10.1021/jp102635s
83. Benny J, Liu J. Spin-orbit charge transfer from guanine and 9-methylguanine radical cations to nitric oxide radicals and the induced triplet-to-singlet intersystem crossing. *J Chem Phys* 2023;**159**:085102. https://doi.org/10.1063/5.0160921
84. Alecu IM, Zheng J, Zhao Y *et al.* Computational thermochemistry: scale factor databases and scale factors for vibrational frequencies obtained from electronic model chemistries. *J Chem Theory Comput* 2010;**6**:2872–87. https://doi.org/10.1021/ct100326h
85. Riplinger C, Sandhoefer B, Hansen A *et al.* Natural triple excitations in local coupled cluster calculations with pair natural orbitals. *J Chem Phys* 2013;**139**:134101. https://doi.org/10.1063/1.4821834
86. Guo Y, Riplinger C, Becker U *et al.* Communication: an improved linear scaling perturbative triples correction for the domain based local pair-natural orbital based singles and doubles coupled cluster method [DLPNO-CCSD(T)]. *J Chem Phys* 2018;**148**:011101. https://doi.org/10.1063/1.5011798
87. Neese F. The ORCA program system. *Wiley Interdiscip Rev: Comput Mol Sci* 2012;**2**:73–8. https://doi.org/10.1002/wcms.81
88. Neese F. Software update: the ORCA program system, version 4.0. *WIREs Comput Mol Sci* 2018;**8**:e1327. https://doi.org/10.1002/wcms.1327
89. Marcus RA. Unimolecular dissociations and free radical recombination reactions. *J Chem Phys* 1952;**20**:359–64. https://doi.org/10.1063/1.1700424
90. Zhu L, Hase WL. A General RRKM Program (QCPE 644). Bloomington: University of Indiana, 1993.

91. Beyer T, Swinehart DF. Algorithm 448: number of multiply-restricted partitions. *Commun ACM* 1973;**16**:379. https://doi.org/10.1145/362248.362275
92. Rodgers MT, Ervin KM, Armentrout PB. Statistical modeling of collision-induced dissociation thresholds. *J Chem Phys* 1997;**106**:4499–508. https://doi.org/10.1063/1.473494
93. Troe J. Statistical adiabatic channel model of ion-neutral dipole capture rate constants. *Chem Phys Lett* 1985;**122**:425–30. https://doi.org/10.1016/0009-2614(85)87240-7
94. Larriba C, Hogan, CJ Jr. Free molecular collision cross section calculation methods for nanoparticles and complex ions with energy accommodation. *J Comput Phys* 2013;**251**:344–63. https://doi.org/10.1016/j.jcp.2013.05.038
95. Larriba-Andaluz C, Hogan, CJ Jr. Collision cross section calculations for polyatomic ions considering rotating diatomic/linear gas molecules. *J Chem Phys* 2014;**141**:194107. https://doi.org/10.1063/1.4901890
96. Baek SJ, Choi K-W, Choi YS *et al.* Spectroscopy and dynamics of methylamine. II. Rotational and vibrational structures of CH_3NH_2 and CH_3ND_2 in cationic d states. *J Chem Phys* 2003;**118**:11040–7. https://doi.org/10.1063/1.1575735
97. Feketeová L, Khairallah GN, Chan B *et al.* Gas-phase infrared spectrum and acidity of the radical cation of 9-methylguanine. *Chem Commun* 2013;**49**:7343–5. https://doi.org/10.1039/c3cc43244k
98. Hunter EP, Lias SG. Evaluated gas phase basicities and proton affinities of molecules: an update. *J Phys Chem Ref Data* 1998;**27**:413–656. https://doi.org/10.1063/1.556018
99. Pratihar S, Ma X, Homayoon Z *et al.* Direct chemical dynamics simulations. *J Am Chem Soc* 2017;**139**:3570–90. https://doi.org/10.1021/jacs.6b12017
100. Bonifačić M, Armstrong DA, Štefanić I *et al.* Kinetic isotope effect for hydrogen abstraction by $^{\bullet}$OH radicals from normal and carbon-deuterated ethyl alcohol and methylamine in aqueous solutions. *J Phys Chem B* 2003;**107**:7268–76. https://doi.org/10.1021/jp027790e
101. Wigner E. Crossing of potential thresholds in chemical reactions. *Z Physik Chem* 1932;**B19**:203–16. https://doi.org/10.1515/zpch-1932-1920
102. Wen T, Zhao S, Stingele J *et al.* Quantification of intracellular DNA–protein cross-links with N7-methyl-2′-deoxyguanosine and their contribution to cytotoxicity. *Chem Res Toxicol* 2024;**37**:814–23. https://doi.org/10.1021/acs.chemrestox.4c00076

Received: December 9, 2024. **Revised:** January 21, 2025. **Editorial Decision:** January 23, 2025. **Accepted:** January 28, 2025